"Effects of transition metal dopants on the calcination of CaCO3 under Ar, H_2O and H_2."
T.T. Belete, M.C.M van de Sanden and M.A. Gleeson. Journal of CO_2 Utilization 31 (2019) 152–166
https://doi.org/10.1016/j.jcou.2019.03.006

Effects of transition metal dopants on the calcination of $CaCO_3$ under Ar, H_2O and H_2

T.T. Belete, M.C.M van de Sanden and M.A. Gleeson.

DIFFER - Dutch Institute for Fundamental Energy Research, De Zaale 20,

5612 AJ Eindhoven, the Netherlands.

Keywords: Calcium carbonate, Thermal decomposition, Transition metals, CO_2 conversion, Water vapour, Hydrogen.

Abstract

This study compares thermal decomposition of pure and transition metal-doped (Fe, Co, Ni, Cu, Zn) calcium carbonate samples under ~0.1 mbar of Ar, H_2O, and H_2 in order to evaluate the effects of doping on CO_2 release and conversion.

All samples were synthesized via precipitation methods at room temperature from calcium chloride and sodium carbonate precursors, with additional doping of the relevant transition metal chloride. Structural and compositional analysis of the as-prepared and calcined materials is presented. TM-doping results in an earlier onset of CO_2 release as compared to Pure $CaCO_3$ irrespective of calcination gas. Cu-doping induced the largest temperature reduction. Calcination in H_2O produces an additional lowering of the release temperature, as compared with calcination in Ar, with the Zn-doped sample exhibiting the largest enhancement. During calcination in H_2, the Ni-, Co- and Fe-doped samples produce a significant enhancement of CO_2 to CO conversion, while the overall conversion by the Cu- and Zn-doped samples remained comparable to that of Pure $CaCO_3$. The Ni-doped samples, which produced the highest CO_2 conversion, showed the largest relative enhancement when the calcination gas was changed to H_2.

1. Introduction

Combustion of fossil fuels to meet energy demands results in large quantities of CO_2 being released into the atmosphere, leading to adverse effects on the global climate [1]. In order to ensure both a sustainable environment and economy, transitioning from fossil fuels to renewable energy sources is necessary. However, given their current scale of usage, fossils fuel will remain a substantial component of the energy mix in the near-term [2], [3]. Thus, in light of ambitions of limiting the global average surface temperature rise relative to pre-industrial levels, deployment of carbon capture processes to counteract industrial emissions may be crucial. CO_2 captured from industrial plants can be subsequently stored in geological formations or may be used as a feedstock for the chemical and other industries. This approach can assist in reducing emission in the short-to-medium term, thereby facilitating a smooth transition to a long-term sustainable energy system.

A relatively cost effective and well-established technology for CO_2 capture is the Calcium Looping (CaL) process [4]–[7] first proposed by Shimizu *et al*.[8] This cycle uses low cost and abundant calcium carbonate ($CaCO_3$) as the base material to capture CO_2 in a solid-sorbent cycle [4], [9]. It is described by the reversible reaction:

$$CaO(s) + CO_2(g) \Leftrightarrow CaCO_3\ (s)\ \Delta H_{298K} = \pm 178 KJ/mol \quad (1)$$

In the forward reaction, referred to as carbonation, CO_2 from flue gas reacts with CaO. Although this is an exothermic reaction, it is typically performed at a temperature in the 600-650°C range in order to accelerate the reaction kinetics [4], [8]. The reverse reaction to yield a nearly pure CO_2 stream, referred to as calcination, is typically performed in the temperature range 850-950°C [5], [6], [10]. Calcium looping has potential to contribute to de-carbonization of industrial plants (gas-

and coal-fired power plants, biomass power plants, and cement and steel manufacturers) [11]–[14]. The main drawbacks of the process are the energy penalties associated with the elevated temperature required for both the capture and the release components of the cycle, and a decreasing CO_2 carrying-capacity over repeated adsorption-desorption cycles due to thermally-induced sintering and pore closure of the material [4], [15].

Improving the performance of the CaL cycle has become an important research goal over recent decades. The selective addition of water (steam) at different points in the cycle has been demonstrated to have a beneficial effect on the overall performance [16], [17]. For instance, Manovic *et al*. [18] evaluated carbonation of CaO obtained through calcination of limestones from different geographical origins in 20% steam and improved the cyclability of CaO for CO_2 absorption. Lin *et al*. [19] reported an increase of 30% in adsorption capacity in 60% steam at 920°C relative to adsorption in pure CO_2 at 1020°C.

An interesting observation, first reported by Reller *et al.* [20], is that thermal decomposition of $CaCO_3$ in 1.0 bar of H_2 resulted in both a reduction in the decomposition temperature and in the direct production of CO. This and a follow-up report (Padeste *et al*. [21]) also demonstrated that the inclusion of transition metal (TM) additives in calcium carbonate could either enhance the selectivity toward CO production (Fe, Cu, Ag), or result in direct CH_4 formation with high selectivity (Ni, Ru, Rh). The fact that H_2 is consumed in this process is obviously an issue from any application perspective since it is a valuable energy carrier in its own right. Additionally, it is not readily available in large volumes from sustainable sources. However, direct conversion of CO_2 during the calcination step is an interesting prospect from the perspective of CO_2 utilization. The

simultaneous lowering of the carbonate decomposition temperature is highly desirable since it reduces the associated energy penalty and potentially reduces the rate of sintering.

The reports on $CaCO_3$ decomposition under hydrogen stimulated us to initiate research on the effects of decomposing $CaCO_3$ while exposing the material to a water plasma. The rationale is that the reported positive effects of water addition to the CaL cycle might be further enhanced by plasma excitation of the water molecules. Furthermore, since plasma formation can provide "on-demand" *in-situ* production of H_2, the prospect of inducing direct conversion similar to that observed when decomposing under pure H_2 arises. From an application perspective, H_2 would in this case be derived from H_2O using renewable electrical energy as an input. As a first step in this on-going research, the objective of the current paper is to present an evaluation of the effects that transition metal dopants (Fe, Co, Ni, Cu, and Zn) have on the reactivity and thermal decomposition of $CaCO_3$. Plasma exposures do not form part of this paper, but the decomposition reactor and the typical decomposition conditions used (~0.1 mbar Ar, H_2O, and H_2) are comparable to the conditions used during our plasma exposures. Although this paper is intended to provide a reference point for subsequent work, the effects of TM-doping are interesting in their own right. Most notably, the TM additives induce earlier release of CO_2 relative to the pure $CaCO_3$ irrespective of the chemical nature of the calcining environment. The CO_2 conversion performance of the different dopants in the presence of H_2 is evaluated.

2. Experimental Methods

2.1. Sample Synthesis

All $CaCO_3$ samples were prepared in-house by precipitation methods. Precipitation of inorganic salt from a homogeneous solution of two or more soluble salts is one of the trivial methods by which ions in a liquid solution transforms to crystalline particles. Analytical grade commercial precursors $CaCl_2 \bullet 2H_2O$, Na_2CO_3, $CoCl_2 \bullet 6H_2O$; $FeCl_3 \bullet 6H_2O$; $NiCl_2 \bullet 6H_2O$; $CuCl_2 \bullet 2H_2O$; and $ZnCl_2$ (Sigma-Aldrich, Germany) were used as the synthesis precursors. Pure $CaCO_3$ was prepared by mixing 0.8 M $CaCl_2 \bullet 2H_2O$ solution and 0.8 M Na_2CO_3 solution [22] at room temperature (20-23°C). For the synthesis of the Co, Ni, and Fe-doped samples, the relevant TM chloride amounting to 2.5wt.% of the $CaCl_2 \bullet 2H_2O$ was added to the initial chloride solution (see Table 1 for an overview of synthesis solution compositions). To initiate precipitation, the chloride-containing solution was poured with continuous stirring into a beaker containing the carbonate solution. The inception of carbonate precipitation was immediate in all cases. The mixed solution was stirred for 10-15 minutes to stimulated complete precipitation.

Attempts to precipitate the Cu- and Zn-doped carbonates from solution in a similar manner were unsuccessful. Precipitation was not observed even after prolonged stirring and increasing the temperature to 60°C in an effort to stimulate particle growth. UV-Visible spectroscopy tests performed after 2 hours to detect evidence of particle growth exhibited no absorbance peaks. The presence of foreign ions or other substances can change the precipitation rate of $CaCO_3$ [23] and in the case of Zn and Cu the effect is inhibitive. Trace amounts of zinc(II) and copper(II) are used to control $CaCO_3$ scale deposition in water supply pipes and heat exchangers [24]. Zeppenfeld reported that the presence of Cu and Zn species inhibit calcite growth by blocking

active growth sites [24]. As a consequence, the Cu- and Zn-doped $CaCO_3$ samples were prepared by fast mixing of separately prepared pure TM- and pure Ca-carbonate precipitation solutions. Table 2 gives an overview of the precursor solutions used to synthesize these samples. The two carbonate solutions were combined within 10 seconds of their individual mixing in order to minimize separate growth of $CaCO_3$ and $TMCO_3$ particles. The combined carbonate solutions were stirred for 30 minutes to stimulate complete precipitation.

Following precipitation, all solutions were filtered through filter paper (Whatman) with a pore size of 25 µm and the solids were washed repeatedly with deionized-water. The samples were then dried in an oven for several hours at 65-150°C.

Table 1: Molar concentrations (M) and volume of di-water (ml) of the precursor solutions Pure, Fe-, Co- and Ni-doped $CaCO_3$ synthesis.

$CaCO_3$ sample	**Chloride solutions**		**Carbonate solutions Na_2CO_3**	**TM:Ca molar ratio**
	$CaCl_2.2H_2O$	**TM chloride**		
Pure	0.8M [250ml]	-	0.8M [250ml]	-
Fe-doped	0.81M [150ml]	**$FeCl_3•6H_2O$** - 0.08M [25ml]	0.83M [150ml]	0.014
Co-doped	0.8M [150ml]	**$CoCl_2•6H_2O$** - 0.08M [25ml]	0.83M [150ml]	0.016
Ni-doped	1.22M [200ml]	**$NiCl_2•6H_2O$** - 0.08M [50ml]	1.25M [200ml]	0.015

Table 2: Molar concentrations (M) and volume of di-water (ml) of the precursor solutions Cu- and Zn-doped $CaCO_3$ synthesis.

$CaCO_3$ Sample	**Calcium carbonate solutions**		**TM carbonate solutions**		**TM:Ca molar ratio**
	$CaCl_2.2H_2O$	**Na_2CO_3**	**TM chloride**	**Na_2CO_3**	
Cu-doped	0.73M [100ml]	0.72M [100ml]	**$CuCl_2•2H_2O$** - 0.075M [25ml]	0.1 M [25ml]	0.022
Zn-doped	0.97M [150ml]	0.96M [150ml]	**$ZnCl_2$** - 0.16M [25ml]	0.21M [25ml]	0.027

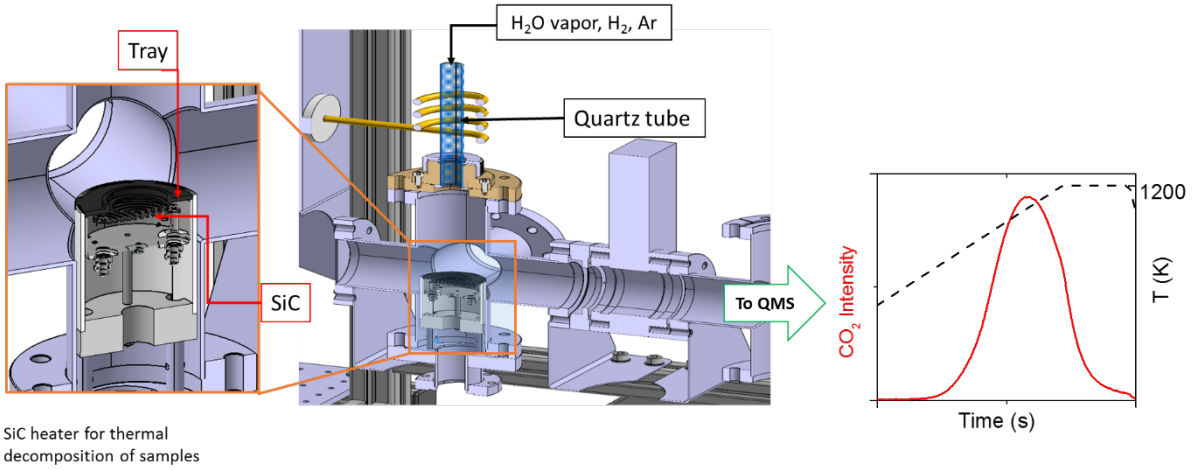

Figure 1: Experimental setup used for calcination of $CaCO_3$ samples. The graph illustrates a measured CO_2 release profile in response to an applied heating profile.

2.2. Experimental setup

Thermal decomposition of the carbonate samples was performed in a vacuum vessel as depicted in Figure 1. It consists of three sections with different operating pressures. Section 1 is the sample compartment (base pressure ~10^{-4} mbar; working pressures up to ~10 mbar) containing a commercial resistive heating stage with a 25.4 mm diameter silicon carbide heating element (UHV-design). The sample is held above the heating element in a circular tray made of Titanium-Zirconium-Molybdenum (TZM) alloy. Ar or H_2 could be introduced to this section by means of a flow controller. Water vapour was introduced via a needle valve from a stainless steel reservoir to achieve the desired target pressure (typically ~0.1 mbar). The deionized water in this reservoir was degassed via several freeze-pump-thaw cycles before use. To maintain a constant pressure of water vapour from the reservoir, it was stabilized at 26°C using a water bath (PolyScience).

Section 2 has a base pressure of ~10^{-8} mbar. It is separated from the sample section by a 200 µm aperture and could be fully isolated by means of a pneumatic valve. This section acts as a gas buffer chamber between Sections 1 and 3. Section 3 (base pressure ~10^{-9} mbar) is separated from Section 2 by a 2 mm aperture. It contains a Quadrupole Mass Spectrometer (QMS Hiden Analytical

HALO). When the pneumatic valve is open, the ionizer of the QMS is in direct line-of-sight of Section 1 via the two apertures. The QMS is used to monitor the time evolution of selected gases (both introduced and evolved from the sample) during decomposition. In the current work the most relevant masses tracked correspond to those of H_2, H_2O, CO, CO_2 and Ar.

2.3. Calcination and Characterization

Typically, 150±1.0 mg of synthesized sample was used in each calcination test. Decompositions were performed by ramping the temperature linearly to 1200 K at a rate of 1 K/s followed by holding at 1200 K for 3 minutes. The temperature is measured by a K-type thermocouple mounted in a fixed position near the sample tray. It is controlled by a custom-built controller with a PID feedback system. As-prepared and calcined samples were characterized by:

X-ray diffraction (XRD): (D8 advance Eco, Bruker, Karlsruhe, Germany) Cu-Kα radiation source (λ=1.5406 Å) at 40 keV and 25 mA was used. Diffraction patterns were collected in Bragg-Brentano θ/2θ geometry in the range of 20°≤2θ≤60°, with scanning step of 0.02°. Qualitative identification of phases was performed using Match! software (Crystal Impact, Bonn, Germany) and quantitative analysis (amount of different phases) by running Rietveld refinements from within Match!, with the actual calculations being automatically performed using the program FullProf [25] in the background. Prior to phase identification, $K_{\alpha 2}$ stripping correction and peak fitting to a pseudo-Voigt function was performed. To identify the phase of the samples, experimental data profile fitting calculations were performed using the peak data as a parameter in constrained least-squares refinement. Finally, the entries from Crystallography Open Database (COD) matching the profile were selected.

Diffuse Reflectance Infrared Fourier Transform Spectroscopy (DRIFTS): A VERTEX 70 FTIR Spectrometer (Bruker, Karlsruhe, Germany) equipped with Praying Mantis DRIFTS cell (Harrick Scientific Corp.) reaction chamber with ZnSe windows was used. The spectrometer has a liquid nitrogen cooled Hg-Cd-Te (MCT) detector. The sample chamber and interferometer were purged with nitrogen to suppress the contribution from atmospheric water vapour and CO_2. The reaction chamber "dome" was pumped to remove CO_2 and H_2O, since it is isolated from the nitrogen purging. The DRIFTS technique offers the potential for non-destructive, simultaneous and real-time measurements of gases and solids. Spectra were collected at room temperature with a resolution of 4 cm^{-1} in the range of 6000-400 cm^{-1}. Each spectrum was averaged over 120 scans. The IR spectra were recorded and stored using OPUS 7.5.18 (Bruker Optics Inc.) spectroscopic software. Prior to measurements, a background spectrum was collected on KBr powder, and all spectra were recorded against this background.

X-Ray Photoelectron Spectroscopy (XPS): A K-Alpha (Thermo Scientific) with Al Kα monochromatic 1486.6 eV X-ray source was used. The measurements were performed on pressed pellets of 2 cm in diameter and quantification was performed by CasaXPS commercial software in which the 2p peaks of TMs are quantified relative to Ca from the same sample.

3. Results and Discussion

3.1. As-prepared samples

Calcium carbonate exists as a various polymorphs: amorphous calcium carbonate (ACC), calcium carbonate hexahydrate, calcium carbonate monohydrate, vaterite, aragonite, and calcite [26]–[30]. Of these, calcite is thermodynamically the most stable [31], [32]. Vaterite and aragonite are the next most stable phases [33], [34]. Calcite, aragonite, and vaterite have a different arrangement of CO_3^{2-} groups, and atoms producing trigonal, orthorhombic, and hexagonal crystal structures, respectively [32], [33], [35], [36].

Figure 2 shows XRD patterns measured from the as-prepared samples used in this study. The patterns reveal the presence of both calcite [as compared with Markgraf *et al*. [37] (space group R-3c, I/I_C=3.7)], and vaterite [as compared with Le bail *et al*. [33] (space group $P6_3/mmc$, I/I_C=1.59)] polymorphs. No evidence of aragonite phase was observed in these samples. Precipitation of aragonite typically requires conditions (temperature; mole fraction) different from those used in the current preparation procedures. Chang *et al.*[38] and Padeste *et al*.[21] reported precipitation of the aragonite phase at synthesis temperatures of 60-80°C. An experimental study by Wada *et al*. [39] on the effects of divalent cations (Fe^{2+}, Ni^{2+}, Co^{2+}, Zn^{2+} and Cu^{2+}) upon nucleation, and growth reported that the formation of aragonite phase is favoured by higher molar ratios of divalent cations. Even though the Cu- and Zn-doped samples were prepared by mixing of the separately prepared individual carbonate solutions, there is no indication of

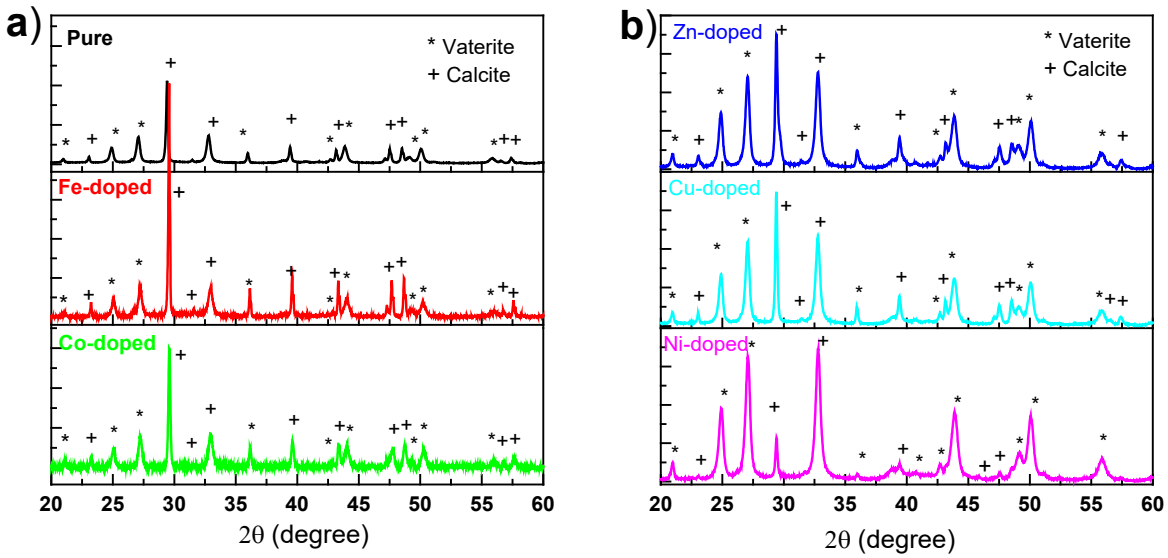

Figure 2: XRD patterns of as-prepared $CaCO_3$ samples: a) Pure, Fe-, and Co-doped, b) Zn-, Cu-, and Ni-doped. Vaterite and calcite peaks are indicated by * and +, respectively.

peaks due $CuCO_3$ or $ZnCO_3$ in the XRD patterns. Given the low fractional content of TMs in the precursor solutions, it is unlikely that pure TM carbonate would be formed in quantities sufficient to rise above the limit-of-detection.

The diffraction patterns were imported to the Match! software to obtain peaks parameters through profile fitting as outlined in the experimental section. Prior to crystallite size calculation, an instrumental standard was created in order to account for and separate the contribution of instrumental peak broadening to the measured peaks. For this the powder diffraction pattern of a corundum (a crystalline form of aluminium oxide) sample was used. The software uses the Scherrer formula [40] (Eq. 2) to calculate the actual crystallite size of selected peaks of interest.

$$L = \frac{K\lambda}{\beta(2\theta)Cos(\theta)} \qquad (2)$$

Where L is crystallite sizes, K is Scherrer constant (0.94), λ is the wavelength (Cu-Kα) (1.5406 Å), β is broadening of the diffraction line at half of the maximum intensity, and θ is the Bragg angle. Therefore, $\beta_{sample} = (FWHM)_{experimental} - (FWHM)_{instrument}$ was used by the software. The overall

average crystallite size was estimated based on the full XRD pattern. The calcite and vaterite average crystallite size were obtained by selecting the respective phase peaks. The resultant determination of the percentage of each phase and of their average crystallite sizes are presented in Table 3.

Vaterite was the dominant phase in the samples co-precipitated with Zn, Cu and Ni, with the Ni-doped sample being almost entirely vaterite. The two phases were approximately equal in the Co-doped sample, while pure and Fe-doped $CaCO_3$ had slightly higher fractions of calcite phase. The average size of calcite crystallites is significantly larger in the samples that are majority calcite (pure and Fe-doped). The average vaterite crystal size does not appear to be dependent on the vaterite crystalline fraction.

Table 3: Percentage and crystallite sizes of calcite and vaterite phases present in the as-prepared samples based upon analysis of XRD spectra.

Precipitated samples	**Average crystallite size (nm)**	**Calcite phase**		**Vaterite phase**	
		%	Average crystallite size (nm)	%	Average crystallite size (nm)
pure	95.2	53.5	129.6	46.5	63.7
Fe-doped	116.3	56.3	190.5	43.7	33.8
Co-doped	59.3	48.4	68.7	51.6	50.0
Zn-doped	41.1	27.0	54.5	73.0	35.5
Cu-doped	55.9	23.7	68.3	76.3	44.4
Ni-doped	57.5	6.2	63.6	93.8	54.9

DRIFTS spectra of the synthesized samples obtained following precipitation and drying are depicted in Figure 3. The measurements confirm the presence of the calcite and vaterite phases as indicated by the XRD patterns. The main vibrational modes observed in the low wavenumber region are assigned as indicated in Table 4. The v_1, v_2, and v_3 values in this work agree to within ±2 cm^{-1} of the values reported in the cited references. Nakamoto *et al*. [41] reports that the mid-infrared spectrum of free carbonate ion has four normal vibrational modes namely, symmetric C-O

stretching mode (v_1), CO_3 out-of-plane stretching mode (v_2), doubly generate asymmetric C=O stretching mode (v_3), and doubly degenerate OCO in-plane bending mode (v_4). In calcite, the v_1 is infrared inactive.

Table 4: Observed vibrational frequencies (cm^{-1}) and associated crystalline phases of $CaCO_3$.

vibrational modes	Wavenumber (cm^{-1})	Phases	References
v_1	*~1088-1090*	*Vaterite*	[27], [42]
v_2	*~850*	*Calcite; Vaterite*	[26], [27], [36]
	~877	*Calcite; Vaterite*	[28], [43], [44]
v_4	*~714*	*Calcite*	[27], [28], [31], [42]
	~746-750	*Vaterite*	[27], [31], [42]

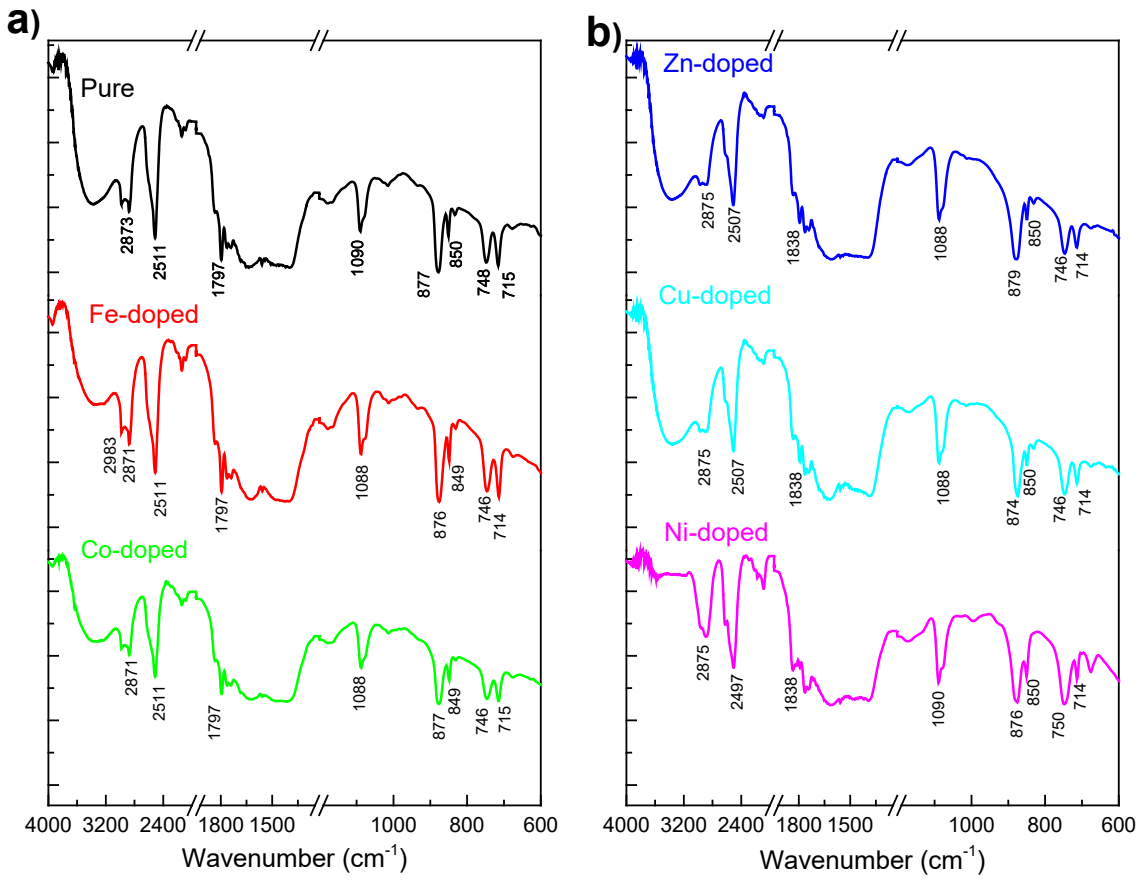

Figure 3: DRIFTS spectra of as-prepared $CaCO_3$ samples: a) pure, Fe- and Co-doped. b) Zn-, Cu- and Ni-doped.

The extremely strong and broad peak observed from 1700-1400 cm^{-1} is C=O asymmetric stretching mode (v_3) of calcite and vaterite; the values are subject to some uncertainty [27]. Flemming *et al*. [42] reported contribution due to the superposition of different modes (v_1 and v_4) with lattice modes in this frequency range. The absorption at 1797 cm^{-1} and 1838 cm^{-1} are overtones band (v_4+v_1). The bands around ~2985-2875 cm^{-1} and 2505-2513 cm^{-1} are harmonic vibrations of C-O bonds [44]. The broad bands in the range of 3700-3000 cm^{-1} are attributed to O-H symmetric stretching and asymmetric stretching of H-O-H from water molecule [43], [45], [46]. The as-prepared Ni-doped sample is noteworthy as being the sole sample that did not exhibit a significant absorbance due to incorporated water.

Some of the as-prepared Pure sample was incrementally heated in a tube furnace to set temperatures in the range from 100-400^{o}C for 1 hour in order to induces the transformation of vaterite to calcite. Vaterite peaks remained evident in the XRD patterns of samples that were

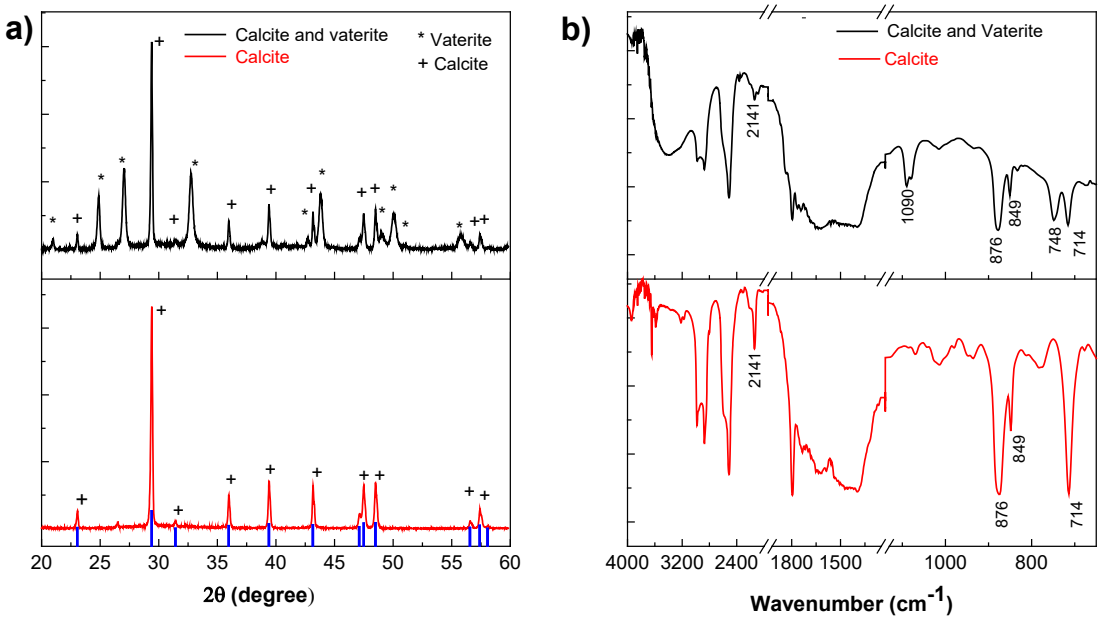

Figure 4: Phase transition of Pure sample from mixed vaterite+calcite to calcite. a) XRD of a sample before (top) and after phase transition (bottom); b) DRIFTS spectra of the sample before (top) and after (bottom) phase transition.

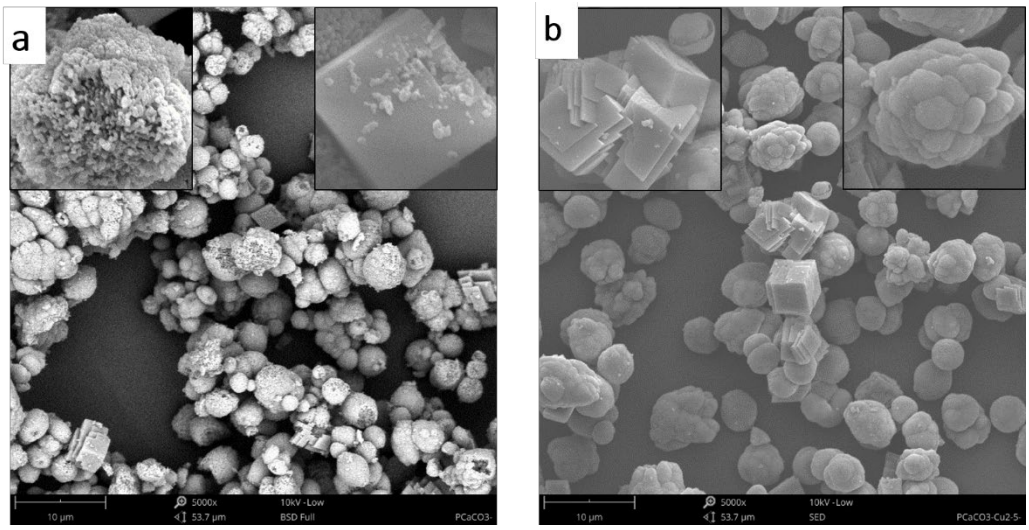

Figure 5: SEM micrograph of as-prepared $CaCO_3$ samples: a) Pure dried at 100°C, b) Cu-doped dried at 100°C

heated up to 325°C. Complete phase transition to calcite was observed in samples after heating to at least 350°C, as illustrated in Figure 4a. The transition temperature observed for our sample is consistent with that of Andrew and Brown, who reported the vaterite-to-calcite phase transition in the range 350-400°C [30]. In Figure 4b, the DRIFTS spectrum of a sample after heating above 350 °C no longer exhibits the vaterite peaks at ~748 cm^{-1} and ~1090 cm^{-1}. Heating also results in removal of the OH vibration band due to adsorbed water molecules (~3700-3000 cm^{-1}). Figures 5 and 6 show SEM images of Pure and TM-doped $CaCO_3$ samples. Figure 5a and b shows as-prepared Pure and Cu-doped $CaCO_3$ samples after drying at 100°C, respectively. Figure 6a shows Pure $CaCO_3$ after drying at 350°C. The effect of the temperature-induced phase transition from mixed calcite+vaterite to pure calcite phase can be seen by comparing Figure 5a (before) and Figure 6a (after). The transition is accompanied by a pronounced morphological change with agglomeration, neck formation and the appearance a smoother and more closed surface.

Figures 6b-d show Co-, Fe- and Ni-doped samples after drying at 100-150°C. The presence of TM doping influences the structure and morphology of the precipitated particles. Cu-doping (Figure

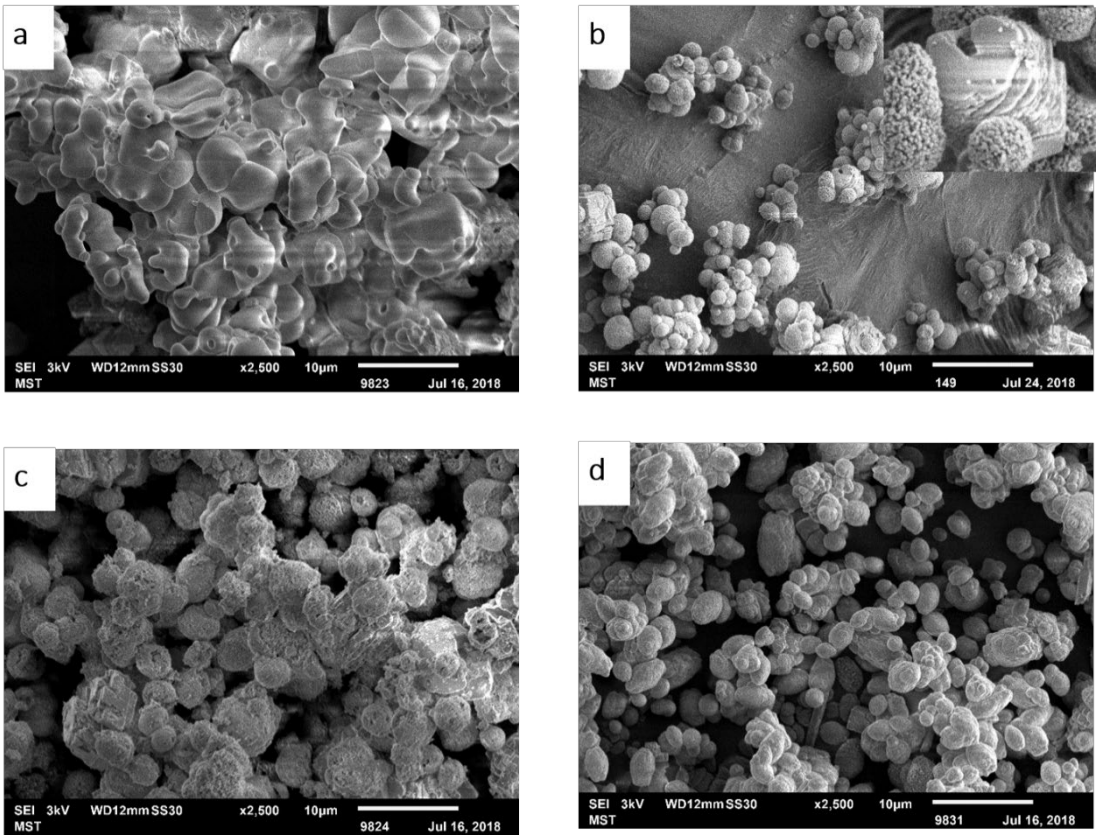

Figure 6: SEM micrograph of as-prepared $CaCO_3$ samples: a) Pure dried at 350°C, b) Co-doped dried at 150°C, c) Fe-doped dried at 150°C, d) Ni-doped dried at 100°C.

5b) appears to increase the occurrence of cubic structures. The Co-doped sample (Figure 6b) exhibits evidence of a layered growth mechanism and a micro-structuring of the more spherical particles. Morphological modification is observed in a number of published works [47]–[49] which suggest that the incorporation of foreign ions during precipitation processes changes the characteristics of different crystallographic phases.

3.2. Sample calcination

Thermal decomposition of ~150 mg of synthesized samples was carried out in the reactor shown in Figure 1 under argon, water vapour and hydrogen gas flows. In all cases the initial pressure in the sample region was ~0.1 mbar. Freshly introduced samples were heated to 1200 K at a rate of

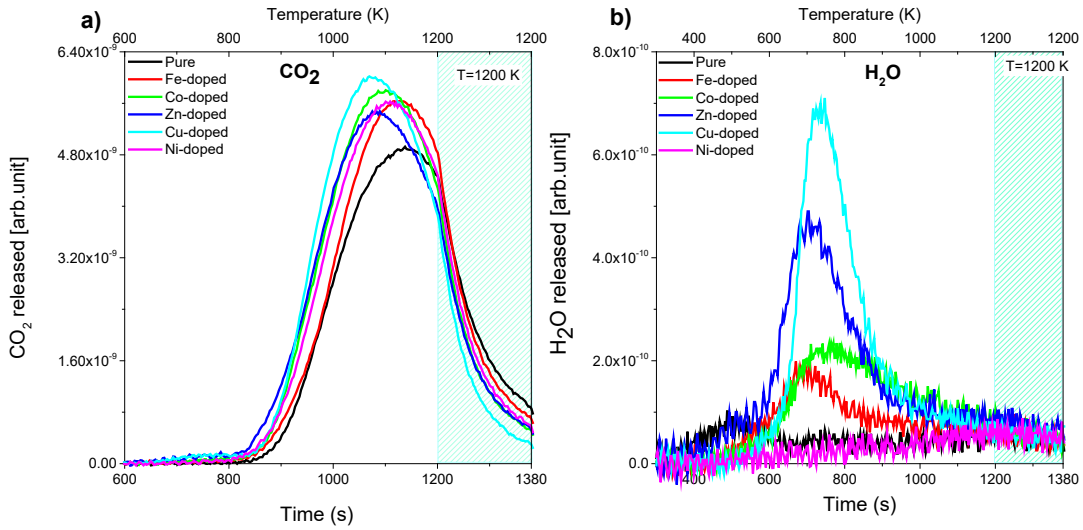

Figure 7: Pure and TM-doped $CaCO_3$ during calcination in ~0.1 mbar Ar atmosphere: a) CO_2 released, b) incorporated H_2O released from each sample. The shaded regions indicate the temperature plateau of 1200 K.

1 K/s and then held at this temperature for 180 s. During calcination heat transfer from the heater to the $CaCO_3$ surface through the sample holder initiates CO_2 release leaving a porous layer of CaO behind. The reaction interface of $CaO/CaCO_3$ moves toward the centre of the particles while CO_2 leave the reaction zone [50]. Heat flow to and CO_2 diffusion from the reaction zone respectively determine the calcination progress [34], [51]. These successive processes result in decomposition of carbonates and formation of CaO particles.

3.2.1. Calcination in argon: Calcination in ~0.1 mbar Ar is a representative case for an unreactive gas. In this case, differences between the decomposition profiles of the various samples can be attributed exclusively to the effects of the TM-additives. Figure 7a shows the CO_2 signal measured during decomposition. In this and subsequent figures, evolved gases are typically plotted against both time (bottom axis) and temperature (top axis). The temperature values used are those recorded from the K-type thermocouple, mounted near the sample tray, that is used to control the heating profile as outlined in the Experimental section.

In all cases the CO_2 evolution increases with temperature, passes through a peak before the maximum sample temperature is reached and then decreases. The decrease in CO_2 evolution while the temperature is still increasing is indicative of the point at which the sample starts to exhibit depletion of CO_2. At this point the combination of remaining CO_2 content, sample structure, and CO_2 diffusion is no longer sufficient to maintain an increasing evolution with increasing temperature. The rate of decrease during the plateau phase (1200-1380 s) and the CO_2 level when heating power is removed (time=1380s) reflect the release rate and final level of depletion of the various samples. Thus, the pure $CaCO_3$ retains the highest level of CO_2 evolution at the completion of the thermal cycle, implying lower fractional conversion to oxide as compared to the TM-doped samples. The Cu-doped sample exhibits the highest conversion to CaO at the end of the heating cycle. The other TM-doped samples are clustered at a roughly equivalent intermediate level.

In the case of some of the TM-doped samples there is a small evolution of CO_2 at somewhat lower temperature prior to the onset of the main CO_2 desorption peak (650-800 K). This was most evident in the case of the Cu- and Zn-doped samples. It is attributed to decomposition of small fractions of pure TM carbonates within these samples. In both cases this early release represented ~1% of the total CO_2 released during the thermal cycle. As outlined above, the Cu- and Zn-doped samples were prepared by mixing of separately prepared carbonate precipitation solutions corresponding to pure $CaCO_3$ and the relevant $TMCO_3$. Consequently, crystallites of the pure TM carbonate have more opportunity to form in the case of these samples. This release was the only direct experimental indication of the possible presence of pure $TMCO_3$ phases.

Comparing the traces shown in Figure 7a, the addition of TM dopants aids the release of CO_2 in all cases. This is evident both from the earlier onset of desorption and from the lowering of the peak-evolution temperature. In general, the order of enhancement is Cu>Zn>Co>Ni>Fe>Pure, although this varies for specific indicators. For instance, Zn-doped $CaCO_3$ shows the earliest onset of the main CO_2 desorption peak, but it is subsequently overtaken by the Cu-doped sample, which exhibits a faster rate of release with increasing temperature. The CO_2 release from the Fe-doped sample is the closest to that of pure $CaCO_3$. The main difference is that at higher temperature (>1000 K) the doped sample is better able to sustain an increasing rate of CO_2 evolution with increasing temperature.

Figure 7b shows high temperature evolution of water from the different samples during the thermal cycle. The samples exhibit different levels of hydration, with the Cu- and Zn-doped samples evolving the highest amount. The fact that the Cu- and Zn-doped samples had the highest water-content may also be related to the different preparation method required to precipitate these samples. The Ni-doped sample is notable for not releasing a significant amount of water during the heating cycle. This is consistent with the infra-red spectrum shown in Figure 3, in which the Ni sample does not exhibit significant OH-related absorption in the 3600-3200 cm^{-1} region. The Pure sample released a comparatively small amount of water in the 400-600 K range. Compared to that sample, the release from the TM-doped samples is generally larger and at a higher temperature.

The earlier and more efficient CO_2 release profiles exhibited by all TM-doped samples suggests that the doping promotes a more open material structure as compared with the pure sample. Incorporated TM dopants may act to destabilize the carbonate lattice. A study conducted by

Reeder *et al*. [52] indicates that divalent transition metal ions occupy six-fold coordinated octahedral sites in the structure of carbonate solids. Trace concentration of divalent Co and Zn in calcite analysed by X-ray absorption fine structure (XAFS) confirmed their substitution in the sixfold coordinated Ca site triggering local distortion [52]. A complete contraction of the structure around Co^{2+} and Zn^{2+} was observed. The incorporation of transition metals into calcium carbonate plays an important role in affecting both thermodynamics and kinetics [49].

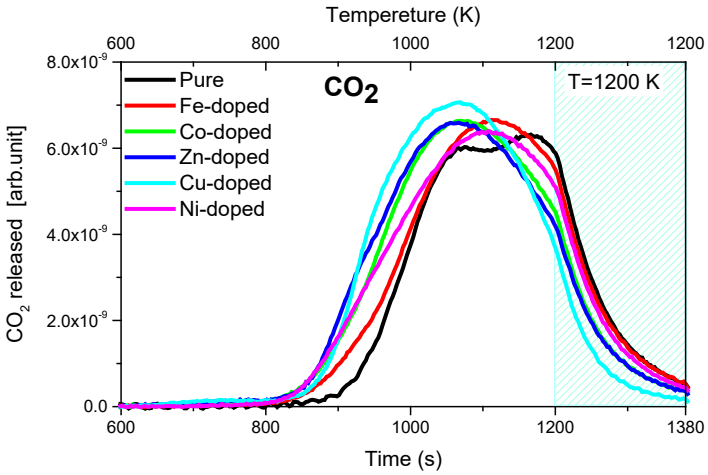

Figure 8: Instantaneous CO_2 released from Pure and TM-doped $CaCO_3$ calcined at 1200 K in ~0.1 mbar water vapour. The shaded region indicates the temperature plateau of 1200 K.

3.2.2. Calcination in water vapour: Calcination in H_2O is also a non-reactive system in terms of $CaCO_3$, although reaction with CaO to form $Ca(OH)_2$ is favoured at lower temperatures [53]. Profiles of CO_2 released from the samples upon calcination in ~0.1 mbar water vapour are plotted in Figure 8. In all cases decomposition under water vapour exhibits improvement relative to decomposition under Ar. In the case of the TM-doped samples, the onset of CO_2 release was ~50 K lower as compared with release in Ar. The effect of water vapour is less pronounced in the case of the pure $CaCO_3$ sample. The initial onset and subsequent temperature-dependent release rate from pure $CaCO_3$ in water vapour is identical to that in Ar. However, once the temperature exceeds ~960 K the rate of release under water vapour exceeds that under Ar. At ~1025 K there

is an interruption with a small decrease in the rate of CO_2 release after which the rate of release increases again. Hence the interruption is not the result of the onset of the CO_2-depletion phase. It may be due to a shift to a diffusion-limited release rate from the sample. Such a switch is not evident during decomposition under Ar, suggesting that its appearance is due to a water-induced acceleration of CO_2 release during the early phase of decomposition is occurring. None of the TM-doped samples exhibit a similar transition during thermal composition. This indicates that the TM doping facilitates CO_2 release over the entire thermal cycle, including enhancing release during the diffusion-limited phase.

Water is known to have a beneficial influence on the calcination of $CaCO_3$ and on the CaL cycle overall. McIntosh et al. [54] reported the presence of water vapour during calcination competes with CO_2 for active sites and improve the reaction rate. Similarly Wang et al.[55] studied the effects of water vapour and CO_2 on the rates of calcite decomposition by using dynamic X-ray diffraction (DXRD) and claimed absorption of water on the active sites ($CaCO_3$*=$CaO.CO_2$) increase decomposition rate by weakening the bond between CaO and CO_2. The effect increases with increasing pressure, but was essentially saturated above ~50 mbar.

3.2.3. Calcination in hydrogen: As first reported by Reller *et al.* [20] and confirmed by subsequent studies [21], [56], decomposition of (TM-doped) $CaCO_3$ in H_2 results in the formation of CO and/or CH_4. The studies indicate good selectivity for methane (Ni, Co) or carbon monoxide (Fe, Cu) production. In addition, a reduction in decomposition temperature is reported. We performed calcination in ~0.1 mbar of H_2 as a comparative benchmark of the reactivity of our sample. Calcination in H_2 was observed to produce H_2O and CO from the reaction of H_2 and CO_2 as shown in Figure 9a and b. The formation of CH_4 was not observed from our samples under the

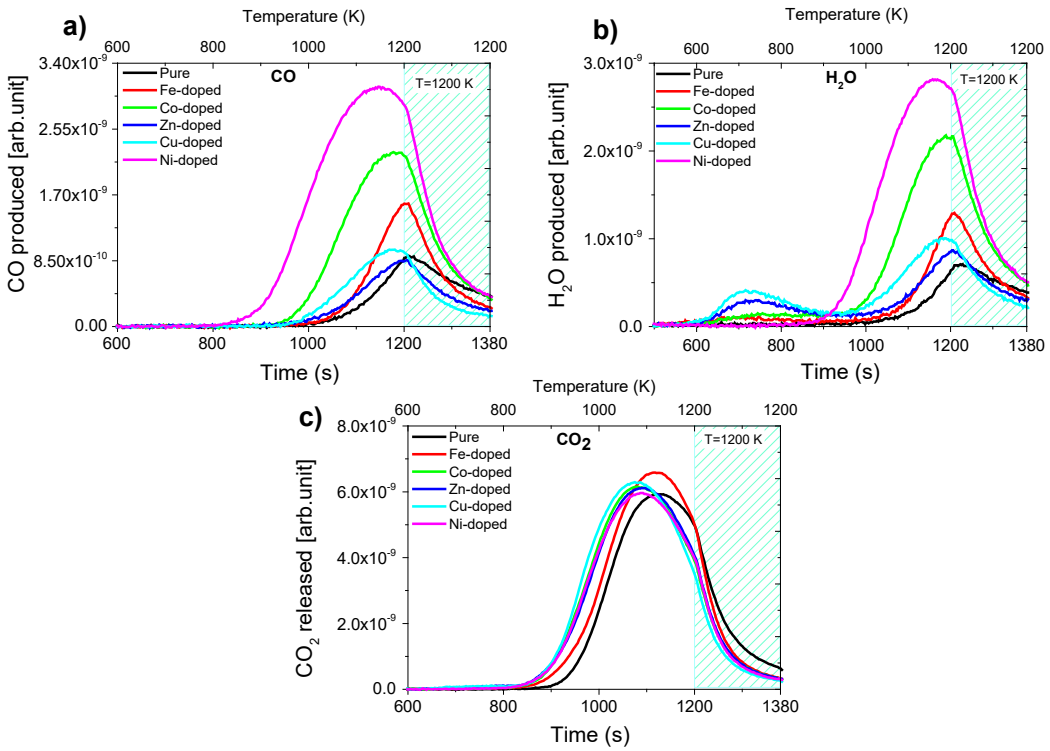

Figure 9: Instantaneous gases evolved from Pure and TM-doped $CaCO_3$ during calcination in ~0.1 mbar H_2. a) CO produced, b) H_2O produced from the reaction of H_2 and CO_2, c) total CO_2 released. The shaded regions indicate the temperature plateau of 1200 K.

current conditions. This is attributed to the low working pressure used, which is not sufficient to allow significant production of CH_4 and thus favours CO formation. CH_4 formation consistent with the earlier reports has been observed from our samples, most notably from the Ni- and Co-doped samples, during thermo-gravimetric analysis under higher partial pressures (~600 mbar) of hydrogen (measurements not shown).

The CO traces shown in Figure 9a have been corrected to remove the contribution from cracking of CO_2 in the mass spectrometer ionizer. All samples, including the pure carbonate, produced CO to some extent. In terms of promoting conversion under the current conditions, Ni-doping was by far the most effective, followed by Co. The effectiveness of production of CO follows the order Ni>Co>Fe. In the case of H_2O traces shown in Figure 9b some of the measured traces have a double peak structure. The lower temperature peaks seen in the 600-900 K region are due to

direct water release from the samples. These H_2O desorption peaks are equivalent to those shown in Figure 7b for calcination in Ar. The higher temperature water peak is the product of the reaction of H_2 and CO_2.

Figure 9c shows the total CO_2 released from the different samples as a function of time (temperature). These traces are obtained by adding the measured CO and CO_2 traces after accounting for the contribution of CO_2 cracking in the QMS ionizer to the CO response and after correcting for the measured difference in relative sensitivity of the CO and CO_2 mass spectrometer response. The release profiles measured from Cu, Zn, Ni, and Co are notable more similar than was the case for calcination under Ar or H_2O. Release from the Fe-doped sample is delayed relative to the other TM-doped samples, but earlier than from the Pure sample. This difference is more clear-cut than was the case for calcination under Ar and H_2O where there was greater similarity between the Pure and Fe-doped samples.

Various studies [20], [21], [57], [58] illustrate the potential of transition metals to act as reduction/hydrogenation catalysts. Accordingly, transition metals mixed in the samples clearly showed their role as internal catalysts during calcination in a hydrogen atmosphere. Thermal decomposition of metal carbonates at high pressures of hydrogen is complex. As illustrated by Reller *et al.* [32], the solid products formed can be metal oxides, mixtures of metal oxides with different oxidation states or elemental transition metals in which the overall reaction could can be written as:

$$MCO_3(s) + (x + y + 4z)H_2(g) \longrightarrow MO_{1-x}(s) + (1 - y - z)CO_2(g) + yCO(g) + zCH_4(g) + (x + y + 2z)H_2O \quad (3)$$

Since CH_4 is not formed in the current study, z=0 and the equation simplifies to:

$$MCO_3(s) + (x+y)H_2(g) \longrightarrow MO_{1-x}(s) + (1-y)CO_2(g) + yCO(g) + (x+y)H_2O \quad (4)$$

This formula has two extrema: *x*=0 represents the formation of metal oxide:

$$MCO_3(s) + yH_2(g) \longrightarrow MO(s) + (1-y)CO_2(g) + yCO(g) + yH_2O \quad (5)$$

and *x*=1 represent the formation of atomic metal:

$$MCO_3(s) + (1+y)H_2(g) \longrightarrow M(s) + (1-y)CO_2(g) + yCO(g) + (1+y)H_2O \quad (6)$$

Reaction 5 can be followed by a direct reduction:

$$MO(s) + H_2(g) \longrightarrow M(s) + H_2O \quad (7)$$

Reactions 5 and 7 combined leads to the same net outcome as Reaction 6. The oxide reduction in Reactions 6 and 7 result in more H_2O than CO formation. If Reaction 5 occurs without subsequent reduction, then the two species are produced in equal amounts.

Figure 10 shows CO:H_2O production ratios from the pure and TM-doped $CaCO_3$ samples. The CO intensity was corrected for the contribution from cracking in the QMS. In the case of H_2O, the

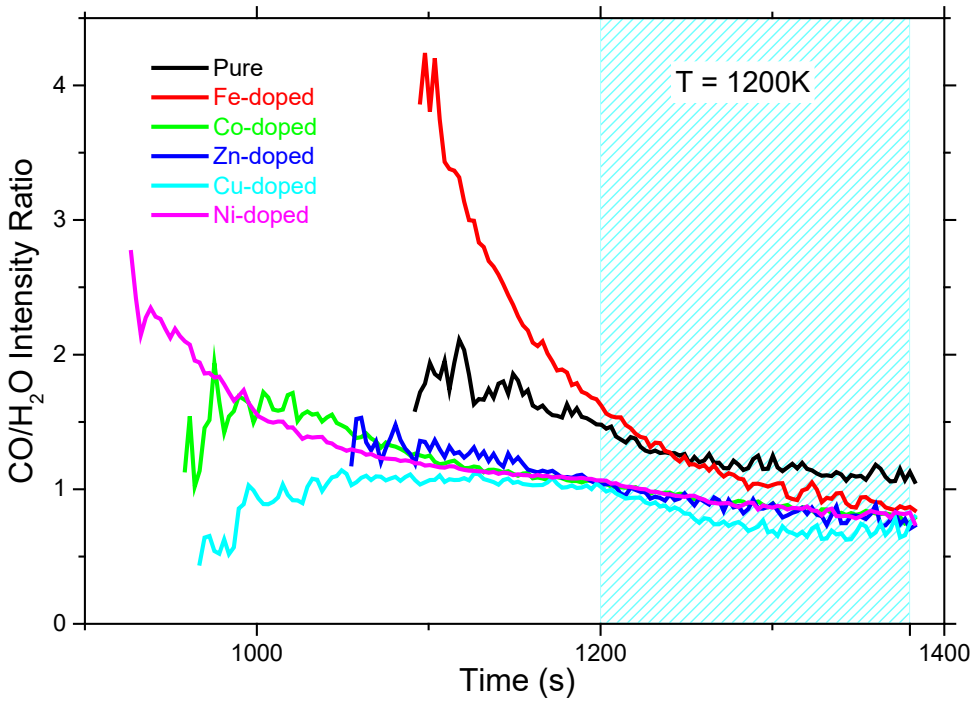

Figure 10: CO:H_2O production ratios as a function of time for the Pure and TM-doped $CaCO_3$ samples. during calcination in ~0.1 mbar H_2. The shaded region indicates the temperature plateau of 1200 K.

traces measured from the Ar-calcined samples were used to correct the H_2-calcined dataset for the contribution from incorporated water. Neither trace was adjusted for the QMS relative sensitivity factor prior to calculating the CO:H_2O ratio. The ratio traces have been truncated to coincide with the approximate onset of CO release

In an ideal reaction scenario, where the only net reaction is $CO_2+H_2 \rightarrow CO+H_2O$, the comparison shown in Figure 10 would be expected to show a straight line of slope=0. While we presume that the Pure sample should be closest to this ideal, it none-the-less shows a slight negative slope. This can be attributed to differences in the system residence time of the evolved gases during calcination. Specifically, an accumulation of H_2O relative to CO will result in a negative slope as a function of time.

Comparing the TM-doped ratios to that of the Pure sample, there are differences in all case, which points to a more complex reaction sequence. The Fe-doped sample has a significantly higher CO:H_2O ratio during the temperature ramp phase. Hence less H_2O than CO is being evolved. This can be accounted for if there is additional oxide formation associated with the Fe-doping while CO is being released. The ratio drops quickly and converges to that of the other TM-doped samples toward the end of the plateau phase. The CO:H_2 ratios of the other TM-doped samples are generally in close agreement with each other and are consistently lower than that of the Pure sample. This indicates extra H_2O evolution relative to CO and may be accounted for by additional TM-induced oxide reduction under a H_2 atmosphere (Reaction (7)).

The fractional conversion of CO_2 to CO is derived from the ratio of the CO produced to the CO_2 released. Figure 11a shows plots of the instantaneous fraction of CO_2 that is converted to CO over the course of the calcination. The Ni-doped sample exhibits significant activity over the full

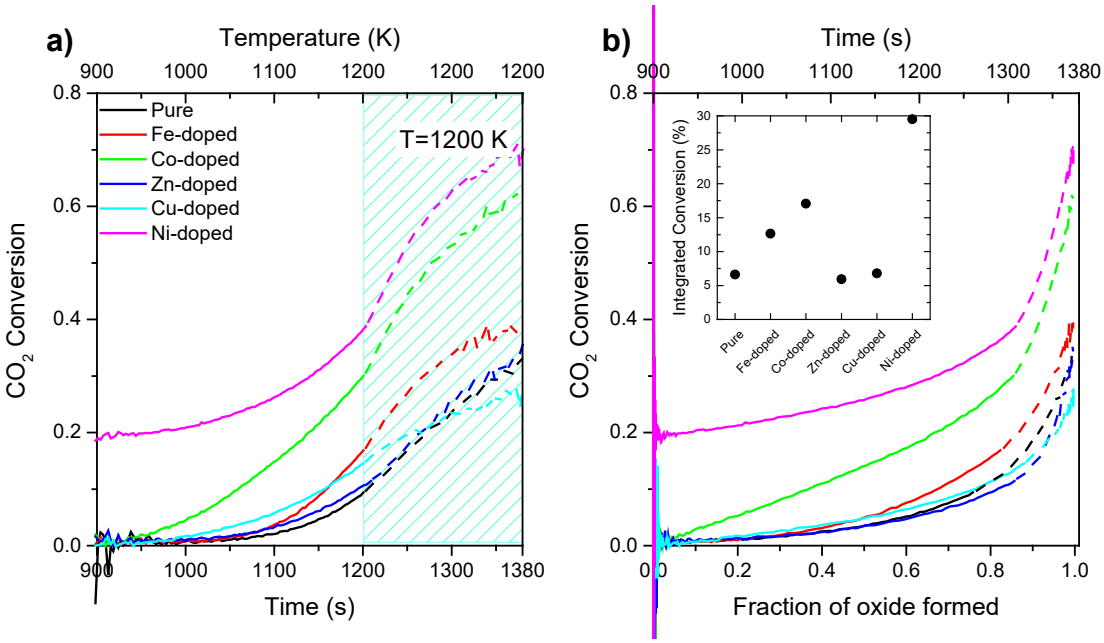

Figure 11: Fraction of CO_2 converted to CO versus a) time and b) fraction of oxide formed during calcination of Pure and TM-doped CaCO3 in ~0.1 mbar H_2. The shaded region and dashed line segments indicate the temperature plateau of 1200 K. The inset in panel b) shows the overall conversion percentage after calcination.

thermal cycle. It produced ~20% conversion at a temperature of 900 K, increasing to~38% at 1200 K. In contract, the activity of the Co-doped sample is initially low but increases rapidly as the calcination proceeds. Conversion increased smoothly from zero to ~30% at 1200 K. The Cu-$CaCO_3$ sample exhibits the third best conversion efficiency at lower temperatures. However, its conversion has a relatively weak dependence on temperature and during the plateau phase of the thermal cycle, it becomes the lowest of all sample.

An estimate of the fractional conversion of carbonate to oxide can be derived from the integrated total released CO_2 traces. This was done on the basis of the Cu-$CaCO_3$ sample and an assumption of 99% conversion at the end of the temperature plateau. Figure 11b illustrates how the CO_2 conversion fraction varies versus the oxide fraction formed. In this case, the transition from the temperature ramp to the temperature plateau is indicated by the change from a solid to a dashed line. In all cases, ~85% oxide formation coincides with a significant increase in the rate of

conversion. For the Ni- and Co-doped samples, in particular, this transition coincides with a pronounced increase in the fractional conversion.

The inset in Figure 11b shows the cumulative CO_2-to-CO conversion percentages over the complete calcination. The most active samples, in decreasing order, were the Ni-, Co- and Fe-doped. Notably, the Cu- and Zn- doped samples performed no better than the Pure sample in terms of overall CO production under the current calcination conditions, although they do perform better at lower temperature.

3.2.4. Calcination cross-comparison: Figure 12 compares the decomposition of the five TM-doped samples relative to the pure sample for calcination under (a) Ar, (b) H_2O, and (c) H_2. This is done on the basis of the temperature required to achieve a comparable fractional amount of oxide formation. Consequently, the temperature difference (ΔT) values plotted on figure 12 relate only to the ramping phase of the calcination. A negative ΔT indicates that a given oxide fraction

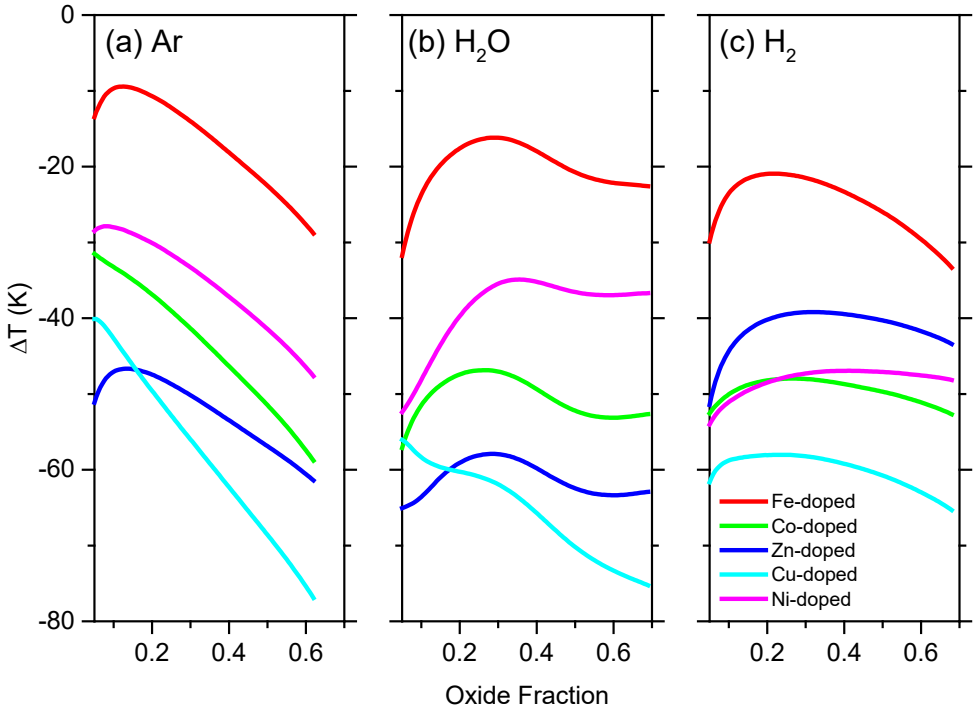

Figure 12: Comparison of the influence of calcination environment (Ar, H_2O and H_2) on the fractional oxide formation during decomposition of the six carbonate samples.

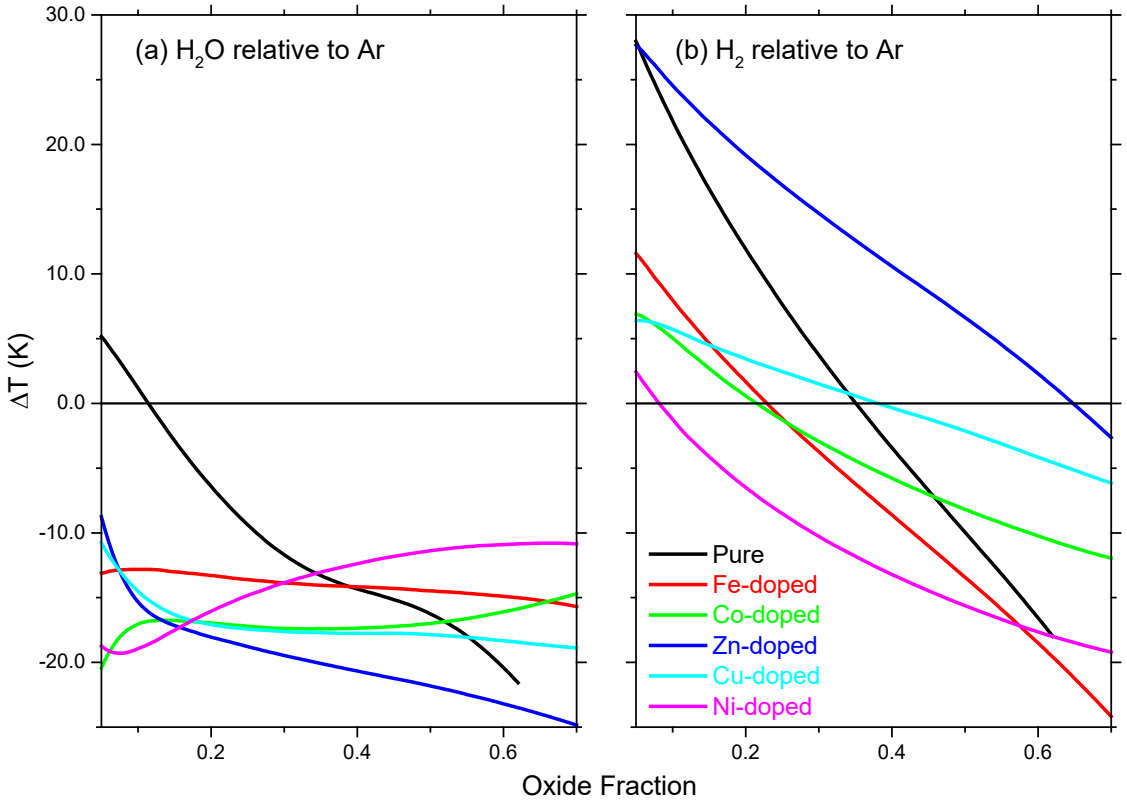

Figure 13: Comparison of the influence of TM-doping on the fractional oxide formation during decomposition under Ar, H_2O and H_2.

is achieve at a lower temperature relative to the Pure sample under the same calcination gas. TM doping improved the performance in all case, with Cu having the greatest effect and Fe the least. In general, when calcined under Ar the performance improves with increasing degree of oxide formation for all dopants. In the case of H_2O the ΔT variation as a function of oxide fraction is more varied, while for H_2 it is comparatively constant. The Ni-doped sample performs better under H_2 than H_2O, while the Zn-doped sample performs worse. The performances of the other three dopants under the two gases is roughly equivalent.

Figure 13 illustrated the influence calcination gas on the temperature required to achieve a given oxide fraction. As for Figures 11 and 12, the fractional oxide formation is based on (and is analogous to) integration of the total CO_2 released, with the release from the Cu-doped samples

at t=1380s in a given atmosphere being assumed to represent 99% conversion. Figure 13a illustrated the performance for H_2O relative to Ar, and Figure 13b shows a similar plot for H_2 relative to Ar. When Ar is replaced by H_2O, all sample show a decrease in the calcination temperature on the order of ~15-20K. Zn-doping is the most improved by the switch to H_2O while the Pure sample is the least affected. In the case of switching from Ar to H_2, the outcome is more mixed. In this case the performance of the Zn-doped sample is significantly worse. All samples perform less well under H_2 during the early stage of the calcination but all improve at higher oxide fraction/higher temperature. This improvement is most pronounced in the case of the Pure and Fe-doped samples.

It is evident from the comparisons shown in Figures 12 and 13 that, under current conditions, TM doping has the most significant and consistent impact on calcination performance irrespective of the ambient gas. Of the five TM dopants tested, doping with Cu has the largest impact on calcination as compared with the pure sample. Although the influence is smaller, use of H_2O does improve calcination relative the Ar case. Calcination in H_2O reduces the decomposition time (temperature) required to produce a given fractional oxide conversion in all cases. The effect is most pronounced for the Zn-doped sample. Calcination in H_2 is generally inferior to calcination in Ar during the early stages of the thermal cycle, particularly in the cases of the Zn-doped and pure samples. However, in the later stages (higher temperature), calcination in H_2 is superior to Ar both in terms of producing a higher conversion at a given temperature and in the final overall conversion fraction achieved. Compared to H_2O, calcination in H_2 is significantly less effective in the case of Zn- and Cu-doping. It is only in the case of Fe-doping, and to a lesser extent Ni-doping,

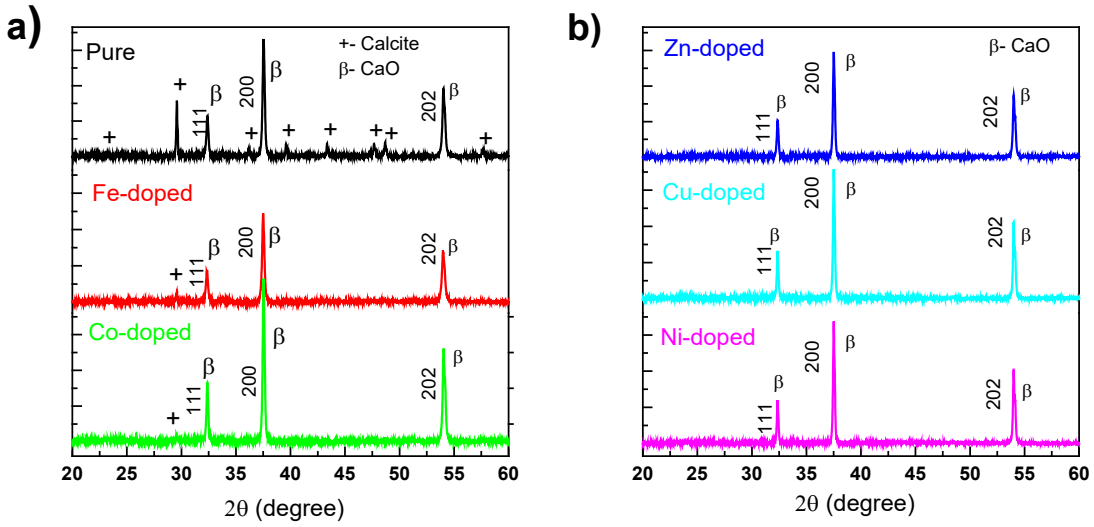

Figure 14: XRD patterns of Pure and TM-doped samples after calcination in ~0.1 mbar H_2O at 1200 K. a) Pure, Fe- and Co-doped samples. b) Zn-, Cu- and Ni-doped samples.

that calcination in H_2 shows a small improvement over calcination in H_2O. The relatively weak effects observed in the current study, compared to the much strong influence of calcination in H_2 seen in previous reports, can again be attributed to the low working pressure.

3.3. Post-calcination characterization

Figure 14 shows XRD patterns of the samples after calcination under water vapour taken shortly after removal from the thermal reactor. The pattern is predominantly CaO in all cases. The most prominent peak position at 2θ=37.34° is correlated to (2 0 0) *hkl* indices cubic structure of CaO, space group Fm-3m (a=4.815Å, density 3.337 g/cm^3). The three main reflections with *hkl* indices of (1 1 1), (2 0 0) and (2 0 2) were used to calculate the crystallite size. Phase analysis and quantification indicate the percentage of CaO formed upon calcination of each sample and the results are shown in Table 5. The XRD patterns confirm that the pure sample has higher $CaCO_3$ (peaks indicated by +) content compared to TM-doped samples calcined under similar experimental conditions. The crystalline phase of the pure sample was ~70%, whereas it was

greater the 90% for all of the TM doped samples. Increasing crystallite size of the calcined samples correlates with higher fractional vaterite content in the original samples. None of the samples exhibited evidence of peaks due to pure TM oxide crystallites.

Table 5: Percentage CaO phase formed and average crystallite sizes from samples after calcination in H_2O at 1200 K. The crystallite sizes of the main peaks of CaO in hkl indices of [111], [200] and [202] are also listed.

Calcined Samples	CaO phase quantity (%)	Average CaO crystallite size (nm)	Crystallite dimension of the main peaks		
			d_{111} (nm)	d_{200} (nm)	d_{202} (nm)
Pure	69.3	60.9	63.4	59.4	56
Fe-doped	93.7	52.1	55.4	54.3	46.8
Co-doped	98.7	70.8	77.5	65.0	69.0
Zn-doped	97.2	79.6	83.2	71.3	84.4
Cu-doped	98.8	78.2	77.3	62.0	95.3
Ni-doped	98.5	106.7	106.4	98.2	115.5

Upon exposure to air, the calcined samples begin to convert to hydroxide form. This transformation occurs on the timescale of hours as is illustrated by the XRD spectra shown in Figure 15. Hydroxide formation was progressive, as illustrated for the Ni-doped sample in Figure 15a. After 45 hours of exposure the hydroxide crystal line fraction was ~63%. Figure 15b

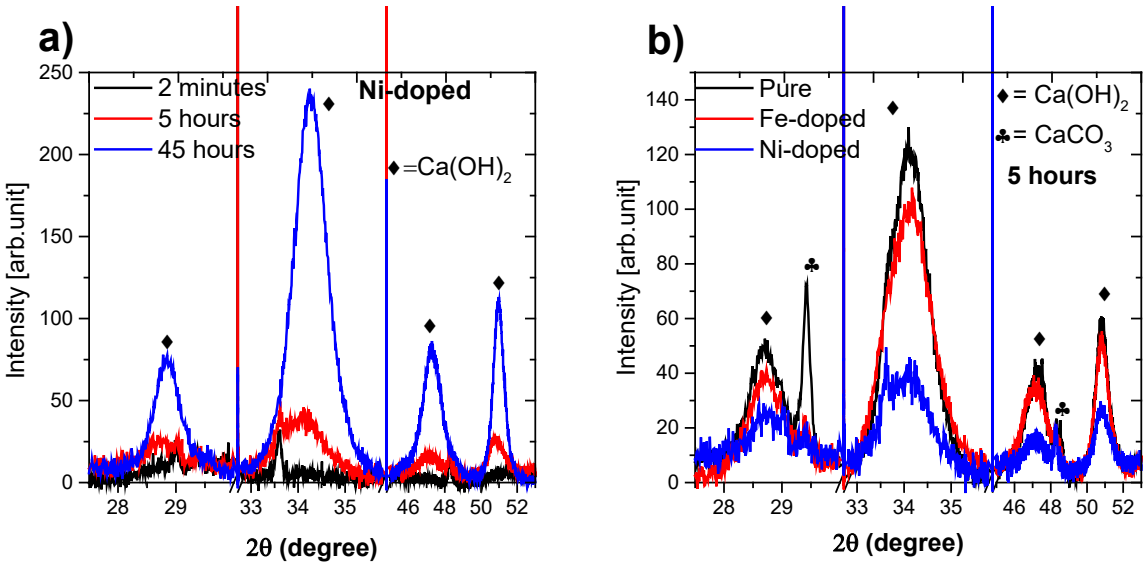

Figure 15:XRD patterns illustrating formation of hydroxide phase through absorption of water vapour from air. a) Time-evolution of Ni-doped sample. b) Pure, Fe and Ni-doped samples after 5 hours.

shows $Ca(OH)_2$-related XRD peaks measured from pure, Fe- and Ni-doped samples after ~5 hours

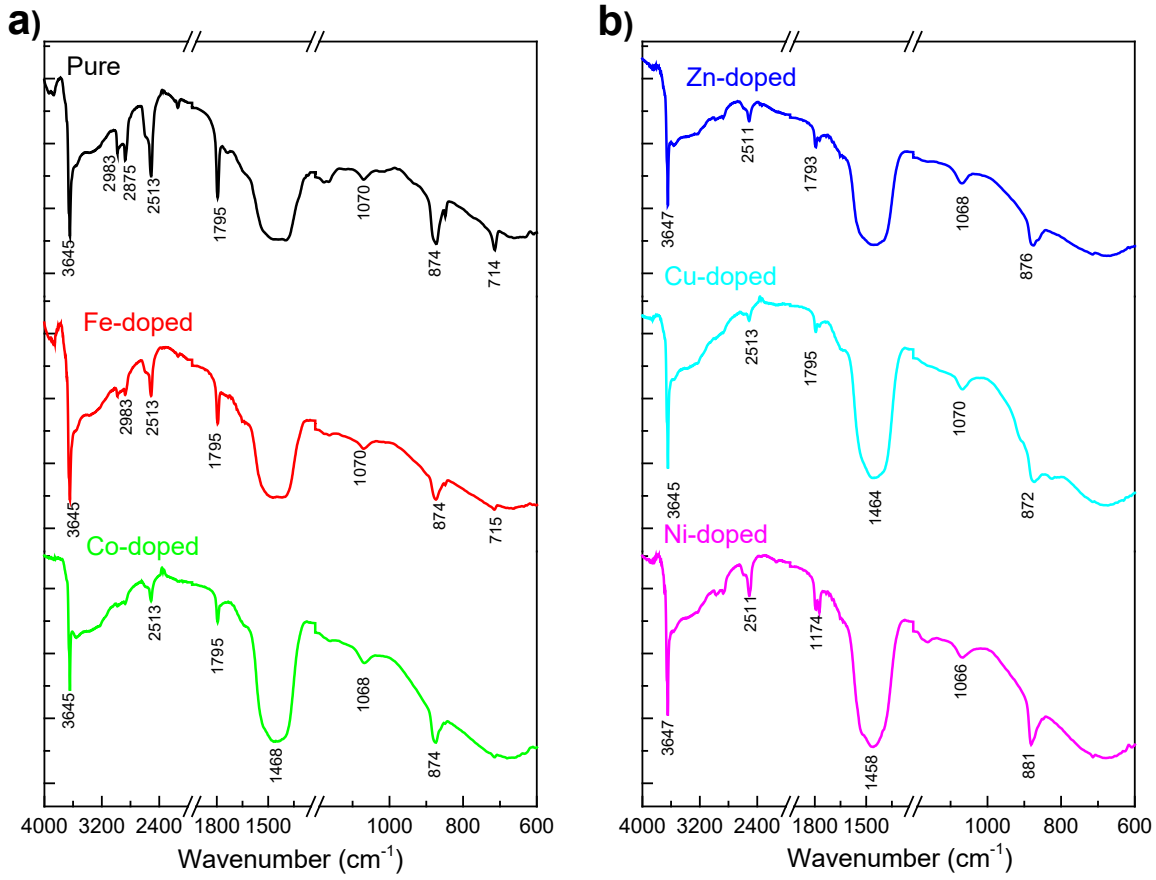

Figure 16:DRIFTS spectra of the post calcined samples in ~0.1mbar H_2O at 1200 K: a) Pure, Fe-, and Co-doped. b) Zn-, Cu- and Ni-doped.

of exposure to atmosphere. The hydroxide crystallite fraction was estimated as ~10.7%, ~13%, and ~4.3%, respectively. Similarly, the Co-doped sample exhibited ~13% hydroxide fraction after ~21 hours of exposure, while the Cu-doped samples had a ~4% fraction after 11 hours. Thus, the TM-dopant has a significant impact on the rate of hydroxide formation under ambient atmospheric conditions.

DRIFTS spectra of the samples after decomposition under ~ 0.1 mbar H_2O are shown in Figure 16. The sharp absorption bands at ~3645-3647 cm^{-1} are the stretching mode of O-H bond in $Ca(OH)_2$ [45], [59], due to atmospheric exposure. Overtone bands observed at 2875 and 2983 cm^{-1} confirm the presence of residual bulk carbonate species in the Pure and Fe-doped samples. The

absorption band at ~2511 cm^{-1} is also related to C-O bonds from carbonate, while the band at 1795 cm^{-1} is due C=O carbonate bond. Broad and strong absorption at ~1500 cm^{-1} corresponds to stretching mode (v_3) of the CO_3^{-2} group. The bands at 1066-1070 cm^{-1} are attributed to symmetric CO stretching, while the bands at 872-881 cm^{-1} corresponds to Ca-O bond [45], [46]. Additionally, the 1774-1795 cm^{-1} bands are attributable to C=O bonds from carbonate. The strong contributions from C-O related bonds in all samples is indicative of surface carbonation after exposure to air.

Figure 17 shows SEM images taken from the Pure and the Co-, Fe- and Ni-doped samples after calcination in water vapour. The pure sample exhibited a globular-type structures with a

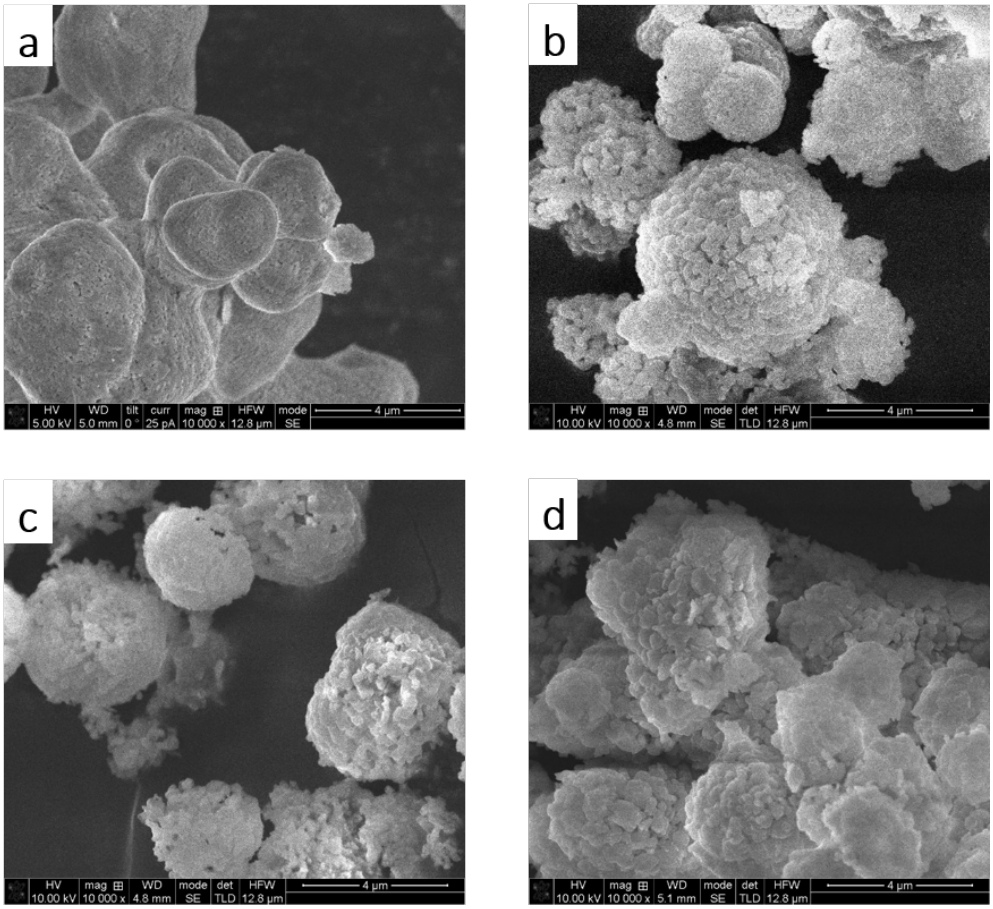

Figure 17: SEM micrograph of samples calcined in ~0.1 mbar H_2O at 1200 K. a) Pure, b) Co-doped c) Fe-doped, d) Ni-doped.

comparatively smooth surface. In comparison, the structures of the TM-doped samples after calcination are significantly more open and there is more micro-structuring of the material. Figure 18 shows corresponding SEM images from these samples after calcination in hydrogen. Structurally, the Co and Ni-doped samples are reasonably similar in the two cases. The biggest differences between decomposition in H_2O and H_2 are in the case of the pure sample, where calcination in H_2 produces a significantly rougher, micro-structured morphology and the Fe-doped sample which exhibits a more "fuzzy" surface structure.

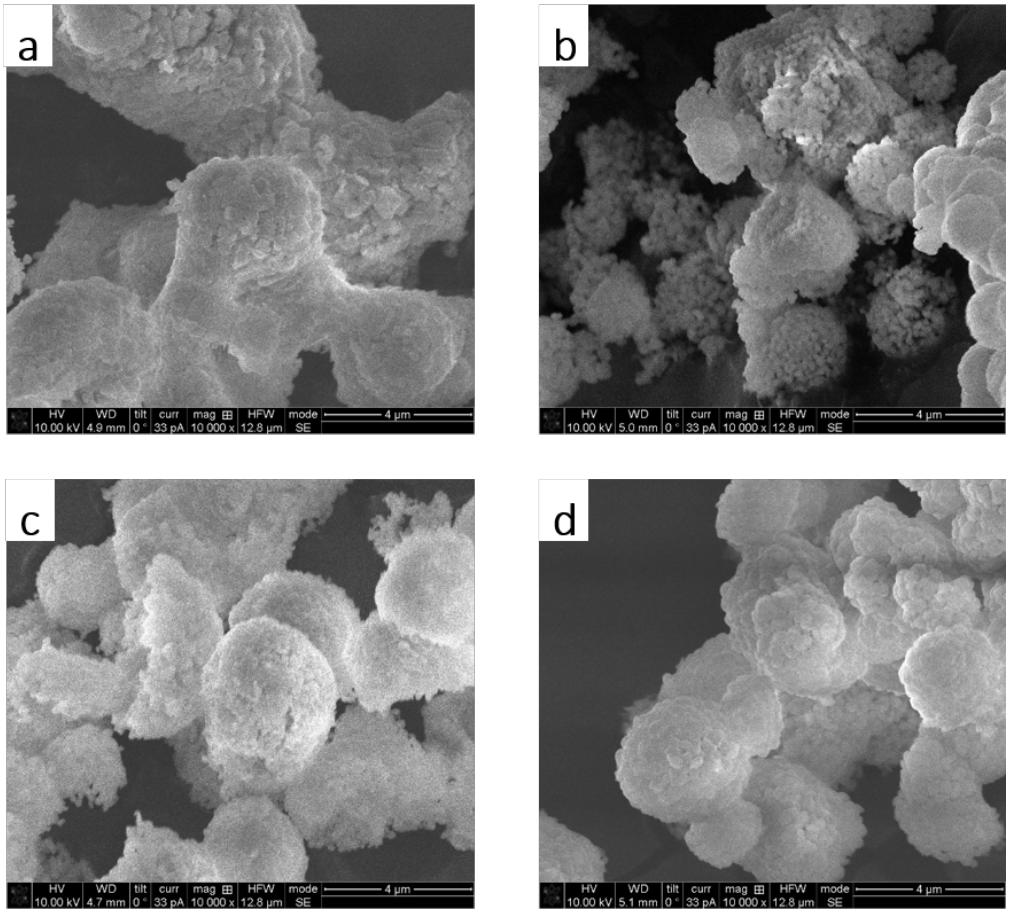

Figure 18: SEM micrograph of samples calcined in ~0.1 mbar H_2 at 1200 K. a) Pure $CaCO_3$, b) Co-doped, c) Fe-doped, d) Ni-doped.

3.4. Composition analysis

X-Ray Photoelectron Spectroscopy measurements were performed to determine the near-surface TM atomic concentration of the as-prepared and Ar-calcined samples. The quantification is based on comparison of the 2p core level peak of the relevant TM to that of Ca from the same sample since the content and distribution of the latter is not expected to be affected by the calcination process. The results are shown in Table 6. These indicate a significant surface enrichment in the case of the as-prepared Cu- and Zn- doped samples. This enrichment is dramatically reduced by the calcination process. In most cases the surface concentration of TM is significantly reduced after calcination. The notable exception is the Co-doped sample, which exhibits a small surface enrichment after calcination.

Table 6: Atomic concentration of transition metals in as-prepared samples and after calcination in Ar, based on XPS analysis.

Sample	Peak analysed	Binding Energy (eV)	TM Concentration As-prepared (at. %)	TM Concentration Calcined (at. %)
Fe-doped	Fe $2p_{3/2}$	710	6.5	1.9
Co-doped	Co $2p_{3/2}$	782	1.3	2.1
Zn-doped	Zn $2p_{3/2}$	1022	9.6	1.4
Cu-doped	Cu $2p_{3/2}$	934	14.0	2.8
Ni-doped	Ni $2p_{3/2}$	854	4.3	0.2

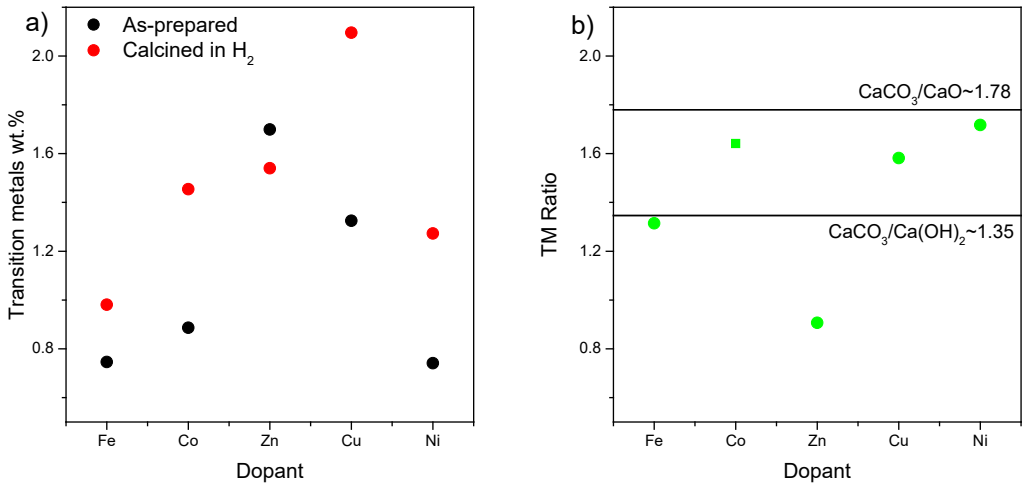

Figure 19: ICP-OES determination of TM content of doped samples (a)TM wt.% of as-prepared and H_2-calcined samples. (b) TM wt.% ratio of H_2-calcined to as-prepared samples.

The bulk composition of TM in the as-prepared and H_2-calcined samples was analysed by Inductively Coupled Plasma Optical Emission Spectrometer (SPECTRO Analytical Instruments GmbH, Germany). Figure 19a shows the resultant TM wt.% in the as-prepared sample and after H_2-calcination. The wt.% values are generally higher in the calcined samples. This is a natural consequence of the release of CO_2 from the sample. Figure 19b shows the ratio of the TM wt.% in the H_2-calcined sample to that of the as-prepared samples. The exact chemical composition of the calcined sample is unclear due to hydroxide formation upon exposure to air. However, we can define two extremes: purely CaO and purely $Ca(OH)_2$. If the content of TM in the sample is unaffected by calcination, then the ratio of the wt.% values should fall between 1.78 (purely CaO) and 1.35 (Pure $Ca(OH)_2$) as indicated on Figure 19b. We discount any contribution from incorporated H_2O in the as-prepared samples and from incomplete calcination or natural CO_2 uptake from air by the calcined sample. For the Fe-, Co-, Ni-, and Cu-doped samples, the post-calcination TM contents are not inconsistent with an unaltered sample content. However, the ratio of the Zn-doped sample indicates a significant decrease after H_2-calcination suggesting loss due to evaporation during the calcination process. Although ZnO is stable up to ~2247K, atomic Zn has much lower melting (~693K) and boiling (~1180K) points than the other transition metals tested. Hence, chemical reduction in the presence of H_2 can account for the observed loss of Zn. This may contribute to the comparatively poor performance of the Zn-doped samples during calcination under H_2.

4. Conclusion

Realising direct conversion of CO_2 during calcination is attractive in terms of process intensification and CO_2 utilization and could simultaneously contribute to improving the calcium looping cycle. To be practical it would require a reliable and sustainable source of H_2, which could in principle be sourced from plasma-dissociated water. As part of evaluating such an approach, we have presented a cross-comparison of the effects of TM-doping on calcium carbonate precipitation and subsequent calcination under low pressure (~0.1 mbar) of Ar, H_2O and H_2.

The addition of TM dopants reduces the decomposition temperature and increases the rate of calcination in all cases. Cu-doping was most effective in this regard while the Fe-doped sample was closest to the pure $CaCO_3$. Reduction of the calcination temperature is desirable in the context of maximizing the efficiency of the calcium looping cycle. It remains to be seen if the performance of doped samples can be maintained over repeated material cycling.

The impact of changing the calcining gas was smaller compared to that of TM doping. Calcining in H_2O improved the performance relative to calcining in Ar in all cases. The largest effect was observed for Zn-doping. Compared to Ar, calcining in H_2 had more mixed results in terms of CO_2 release. It was notably worse in the case of Zn-doping and somewhat better for the Ni-doped sample. The performance under H_2 relative to Ar improved in all cases as the over the course of the calcination.

Direct conversion of CO_2 to CO during calcination under H_2 was enhanced, in order of decreasing effectiveness, by Ni-, Co- and Fe-doping. Cu- and Zn-doping resulted in increased conversion at lower temperature, but did not produce more integrated conversion than the Pure sample. No CH_4 production was observed due to the low working pressure. The measurements indicate that

there is significant additional oxide formation during the early stage calcination of the Fe-doped sample in H_2. Evidence of TM-induced oxide reduction was found for the other samples. The Zn-doped sample showed evidence of TM-loss during calcination under H_2.

Acknowledgements

DIFFER is part of the Dutch institutes organisation of NWO. This work is part of the research programme CO2-Neutral Fuels with project number 13CO23-1, which is partly financed by NWO and supported by Shell. The authors thank assistant professor Nikolay Kosinov from Technical University of Eindhoven, Department of Chemical Engineering and Chemistry for his assistance in arranging ICP-OES measurements. The authors thank Erwin Zoethout for performing the SEM and XPS measurements.

References

[1] V. Masson-Delmotte *et al.*, "Global warming of 1.5°C An IPCC Special Report," 2018.

[2] S. Sarkar *et al.*, "2030 Energy Mix – Key Regional Trends: Marching Towards A Cleaner Future," 2018.

[3] "World Energy Outlook 2017 https://www.iea.org/Textbase/npsum/weo2017SUM.pdf," 2017.

[4] W. Liu *et al.*, "Performance enhancement of calcium oxide sorbents for cyclic CO 2 capture-a review," in *Energy and Fuels*, 2012.

[5] H. C. Mantripragada and E. S. Rubina, "Chemical looping for pre-combustion CO2 capture - Performance and cost analysis," *Energy Procedia*, vol. 37, no. Clc, pp. 618–625, 2013.

[6] I. Martínez, G. Grasa, R. Murillo, B. Arias, and J. C. Abanades, "Kinetics of calcination of partially carbonated particles in a Ca-looping system for CO 2 capture," *Energy and Fuels*, vol. 26, no. 2, pp. 1432–1440, 2012.

[7] G. Ferrara, A. Lanzini, P. Leone, M. T. Ho, and D. E. Wiley, "Exergetic and exergoeconomic analysis of post-combustion CO2capture using MEA-solvent chemical absorption," *Energy*, vol. 130, pp. 113–128, 2017.

[8] T. Shimizu, T. Hirama, H. Hosoda, K. Kitano, M. Inagaki, and K. Tejima, "A Twin Fluid-Bed Reactor for Removal of CO2 from Combustion Processes," *Chem. Eng. Res. Des.*, vol. 77, no. 1, pp. 62–68, 1999.

[9] J. Blamey, N. P. M. Paterson, D. R. Dugwell, P. Stevenson, and P. S. Fennell, "Reactivation of a CaO-based sorbent for CO2 capture from stationary sources," *Proc. Combust. Inst.*, vol. 33, no. 2, pp. 2673–2681, 2011.

[10] M. Broda, R. Pacciani, and C. R. Müller, "CO2 Capture via Cyclic Calcination and Carbonation Reactions," in *Porous Materials for Carbon Dioxide Capture*, A.-H. Lu and S. Dai, Eds. Berlin, Heidelberg: Springer Berlin Heidelberg, 2014, pp. 181–222.

[11] J.Blamey and E.J.Anthony, "End use of lime-based sorbents from calcium looping systems," in *Calcium and Chemical Looping Technology for Power Generation and Carbon Dioxide (CO2) Capture*, P. Fennell and B. Anthony, Eds. Elsevier Ltd., 2015, pp. 153–169.

[12] M.Spinelli *et al.*, "Integration of Ca-Looping Systems for CO2 Capture in Cement Plants," *Energy Procedia*, vol. 114, no. 2, pp. 6206–6214, 2017.

[13] M. C. Romano *et al.*, "The Calcium Looping Process for Low CO2 Emission Cement and Power," *Energy Procedia*, vol. 37, pp. 7091–7099, 2013.

[14] C. C. Cormos and L. Petrescu, "Evaluation of calcium looping as carbon capture option for combustion and gasification power plants," *Energy Procedia*, vol. 51, pp. 154–160, 2013.

[15] R. H. Borgwardt, "Calcium Oxide Sintering in Atmospheres Containing Water and Carbon Dioxide," *Ind. Eng. Chem. Res.*, vol. 28, no. 4, pp. 493–500, 1989.

[16] I. Martinez, G. Grasa, R. Murillo, B. Arias, and J. C. Abanades, "Evaluation of CO2 Carrying Capacity of Reactivated CaO by Hydration," *Energy Fuels*, vol. 25, no. 3, pp. 1294–1301, 2011.

[17] J. Blamey, V. Manovic, E. J. Anthony, D. R. Dugwell, and P. S. Fennell, "On steam hydration of CaO-based sorbent cycled for CO2 capture," *Fuel*, vol. 150, pp. 269–277, 2015.

[18] V. Manovic and E. J. Anthony, "Carbonation of CaO-Based Sorbents Enhanced by Steam Addition," *Ind. Eng. Chem. Res.*, vol. 49, no. 19, pp. 9105–9110, 2010.

[19] S. Lin, T. Kiga, Y. Wang, and K. Nakayama, "Energy analysis of CaCO3 calcination with CO2 capture," *Energy Procedia*, vol. 4, pp. 356–361, 2011.

[20] A. Reller, C. Padeste, and P. Hug, "Formation of organic carbon compounds from metal carbonates," *Nature*, vol. 329, no. 8, pp. 527–529, 1987.

[21] C. Padeste, A. Reller, and H. R. Oswald, "The influence of transition metals on the thermal decomposition of calcium carbonate in hydrogen," *Mater. Res. Bull.*, vol. 25, no. 10, pp. 1299–1305, 1990.

[22] M. A. Popescu, R. Isopescu, C. Matei, G. Fagarasan, and V. Plesu, "Thermal decomposition of calcium carbonate polymorphs precipitated in the presence of ammonia and alkylamines," *Adv. Powder Technol.*, vol. 25, no. 2, pp. 500–507, 2014.

[23] S. Bai, G. Naren, M. Nakano, Y. Okaue, and T. Yokoyama, "Effect of polysilicic acid on the precipitation of calcium carbonate," *Colloids Surfaces A Physicochem. Eng. Asp.*, vol. 445, pp. 54–58, 2014.

[24] K. Zeppenfeld, "Prevention of CaCO3 scale formation by trace amounts of copper (II) in comparison to zinc (II)," *Desalination*, vol. 252, no. 1, pp. 60–65, 2010.

[25] J. Rodríguez-Carvajal, "Recent advances in magnetic structure determination by neutron powder diffraction," *Phys. B Condens. Matter*, vol. 192, pp. 55–69, 1993.

[26] F. Fratini, S.; Signorelli , C.; Peroni , M.; Camaiti, "The presence of vaterite in bonding mortars of marble inlays from Florence Cathedral," *Mineral. Mag.*, vol. 60, pp. 663–665, 1996.

[27] C. E. Weir and E. R. Lippincott, "Infrared studies of aragonite, calcite, and vaterite type structures in the borates, carbonates, and nitrates," *J. Res. Natl. Bur. Stand. Sect. A Phys. Chem.*, vol. 65A, no. 3, pp. 173–183, 1961.

[28] Z. Zhang, Y. Xie, X. Xu, H. Pan, and R. Tang, "Transformation of amorphous calcium carbonate into aragonite," *J. Cryst. Growth*, vol. 343, no. 1, pp. 62–67, 2012.

[29] J. Chen and L. Xiang, "Controllable synthesis of calcium carbonate polymorphs at different temperatures," *Powder Technol.*, vol. 189, no. 1, pp. 64–69, 2009.

[30] R. Babou-Kammoe, S. Hamoudi, F. Larachi, and K. Belkacemi, "Synthesis of CaCO 3 nanoparticles by controlled precipitation of saturated carbonate and calcium nitrate aqueous solutions," *Can. J. Chem. Eng.*, vol. 90, pp. 26–33, 2012.

[31] D. Kralj, L. Brečević, and J. Kontrec, "Vaterite growth and dissolution in aqueous solution III. Kinetics of transformation," *J. Cryst. Growth*, vol. 177, no. 3, pp. 248–257, 1997.

[32] A. Reller, R. Emmenegger, and C. Padeste, "Thermochemical Reactivity of Metal Carbonates," *Chimia (Aarau).*, vol. 45, no. 9, pp. 262–266, 1991.

[33] A. Le Bail, S. Ouhenia, and D. Chateigner, "Microtwinning hypothesis for a more ordered vaterite model," *Powder Diffr.*, vol. 26, no. 01, pp. 16–21, 2011.

[34] A. K. Galwey and M. E. Brown, Eds., "Decomposition of carbonates," in *Thermal Decomposition of Ionic Solids*, vol. 86, Elsevier, 1999, pp. 345–364.

[35] R. Demichelis, P. Raiteri, J. D. Gale, and R. Dovesi, "The Multiple Structures of Vaterite," *Cryst. Growth Des.*, vol. 13, no. 6, pp. 2247–2251, 2013.

[36] J. . Smyth, "The crystal structure of calcite III," *Geophys. Res. Lett.*, vol. 24, no. 13, pp. 1595–1598.

[37] S. Markgraf and R. Reeder, "High-temperature structure refinements of calcite and magnesite," *Am. Miner.*, vol. 70, pp. 590–600, 1985.

[38] R. Chang, S. Kim, S. Lee, S. Choi, M. Kim, and Y. Park, "Calcium Carbonate Precipitation for CO2 Storage and Utilization: A Review of the Carbonate Crystallization and Polymorphism," *Front. Energy Res.*, vol. 5, no. July, pp. 1–12, 2017.

[39] N. Wada, K. Yamashita, and T. Umegaki, "Effects of divalent cations upon nucleation, growth and

transformation of calcium carbonate polymorphs under conditions of double diffusion," *J. Cryst. Growth*, vol. 148, no. 3, pp. 297–304, 1995.

[40] P. Scherrer, "Bestimmung der Größe und der inneren Struktur von Kolloidteilchen mittels Röntgenstrahlen," *Nachrichten von der Gesellschaft der Wissenschaften zu Göttingen, Math. Klasse*, vol. 1918, pp. 98–100.

[41] K. Nakamoto, *Theory of Normal Vibrations*. Wiley-Blackwell, 2008.

[42] F. A. Andersen and L. Brečević, "Infrared Spectra of Amorphous and Crystalline Calcium Carbonate.," *Acta Chemica Scandinavica*, vol. 45. pp. 1018–1024, 1991.

[43] R. J. Gustafsson, A. Orlov, C. L. Badger, P. T. Griffiths, R. a. Cox, and R. M. Lambert, "A comprehensive evaluation of water uptake on atmospherically relevant mineral surfaces," *Atmos. Chem. Phys. Discuss.*, vol. 5, no. 4, pp. 7191–7210, 2005.

[44] M. Galván-Ruiz, J. Hernández, L. Baños, J. Noriega-Montes, and M. E. Rodríguez-garcía, "Characterization of Calcium Carbonate, Calcium Oxide, and Calcium Hydroxide as Starting Point to the Improvement of Lime for Their Use in Construction," *J. Mater. Civ. Eng.*, vol. 21, no. 11, pp. 694–698, 2009.

[45] E. Loste, R. M. Wilson, R. Seshadri, and F. C. Meldrum, "The role of magnesium in stabilising amorphous calcium carbonate and controlling calcite morphologies," *J. Cryst. Growth*, vol. 254, no. 1–2, pp. 206–218, 2003.

[46] M. Ghiasi and A. Malekzadeh, "Synthesis of CaCO 3 nanoparticles via citrate method and sequential preparation of CaO and Ca(OH) 2 nanoparticles," *Cryst. Res. Technol.*, vol. 47, no. 4, pp. 471–478, 2012.

[47] A. L. Braybrook, B. R. Heywood, R. A. Jackson, and K. Pitt, "Parallel computational and experimental studies of the morphological modification of calcium carbonate by cobalt," *J. Cryst. Growth*, vol. 243, no. 2, pp. 336–344, 2002.

[48] L. Fernández-Díaz, J. M. Astilleros, and C. M. Pina, "The morphology of calcite crystals grown in a porous medium doped with divalent cations," *Chem. Geol.*, vol. 225, no. 3–4, pp. 314–321, 2006.

[49] D. Katsikopoulos, Á. Fernández-González, A. C. Prieto, and M. Prieto, "Co-crystallization of Co(II) with calcite: Implications for the mobility of cobalt in aqueous environments," *Chem. Geol.*, vol. 254, no. 1–2, pp. 87–100, 2008.

[50] S. C. N. and F. Frank, "Kinetics of the thermal decomposition of calcium carbonate," *AIChE J.*, vol. 5, no. 1, pp. 115–122.

[51] N. Yoshida, T. Hattori, E. Komai, and T. Wada, "Methane formation by metal-catalyzed hydrogenation of solid calcium carbonate," *Catal. Letters*, vol. 58, no. 2, pp. 119–122, Apr. 1999.

[52] R. J. Reeder, G. M. Lamble, and P. A. Northrup, "XAFS study of the coordination and local relaxation around Co2+, Zn2+, Pb2+, and Ba2+ trace elements in calcite," *Am. Mineral.*, vol. 84, no. 7–8, p. 1049, 1999.

[53] S. Ramkumar and L. S. Fan, "Thermodynamic and experimental analyses of the three-stage calcium looping process," *Ind. Eng. Chem. Res.*, vol. 49, no. 16, pp. 7563–7573, 2010.

[54] R. M. McIntosh, J. H. Sharp, and F. W. Wilburn, "The thermal decomposition of dolomite," *Thermochim. Acta*, vol. 165, no. 2, pp. 281–296, 1990.

[55] Y. Wang and W. J. Thomson, "The Effects of Steam and Carbon-Dioxide on Calcite Decomposition Using Dynamic X-Ray-Diffraction," *Chem. Eng. Sci.*, vol. 50, no. 9, pp. 1373–1382, 1995.

[56] D. Jagadeesan, M. Eswaramoorthy, and C. N. R. Rao, "Investigations of the conversion of inorganic carbonates to methane," *ChemSusChem*, vol. 2, pp. 878 – 882, 2009.

[57] L. Bobrova *et al.*, "Water–Gas Shift Reaction over Ni/CeO2 Catalysts," *Catalysts*, vol. 7, no. 12, p. 310, 2017.

[58] C. S. Chen, W. H. Cheng, and S. S. Lin, "Study of reverse water gas shift reaction by TPD, TPR and CO2 hydrogenation over potassium-promoted Cu/SiO2 catalyst," *Appl. Catal. A Gen.*, vol. 238, no. 1, pp. 55–67, 2002.

[59] A. M. Kalinkin, E. V Kalinkina, O. a Zalkind, and T. I. Makarova, "Chemical Interaction of Calcium Oxide and Calcium Hydroxide with CO2 during Mechanical Activation," *Inorg. Mater.*, vol. 41, no. 10, pp. 1073–1079, 2005.